Detection of Cherenkov Photons Using Silicon Photomultipliers

Masterarbeit
zur Erlangung des akademischen Grades
Master of Science
(M.Sc.)

der Universität Siegen
Naturwissenschaftlich
Technische Fakultät
Department Physik

vorgelegt von
Waleed Khalid

February 6, 2018

Lumos

- J. K. Rowling

Abstract

Compton cameras currently are the best solution to image high-energy gamma rays. Due to competing demands on accuracy and speed, approaches have led to complicated and often bulky designs. To ensure faster imaging of high energy gamma rays, an extension to Compton camera is being researched at University of Siegen which aims to increase overall efficiency by using SiPMs coupled with radiator materials to detect Cherenkov photons from the Compton scattered electron. To ensure the validity of this concept, Cherenkov photons are detected using SiPMs. Some initial studies into Circular Hough Transform for the circle reconstruction of Cherenkov photons are also done.

Contents

Chapter 1

Introduction

Photons have a long history of being used in medicine for imaging purposes. These imaging techniques allow for the visual representation of the interior of a body for diagnostic and therapeutic purposes. The techniques over time have evolved from simple X-ray scans to Computed Tomography (CT) scans to Single-photon emission computed tomography (SPECT) scans. Each consequent technique allows for better reconstruction of the internal structure of a body. CT scans are limited by 2D reconstruction and show how the body looks by using X-ray technology to take measurements from different angles. Whereas, SPECT scans work by imaging the gammas emitted from radioisotopes and are capable of showing a 3D representation of the internal organs. In comparison to CT scans, SPECT scans focus more on how the body works.

Most SPECT imaging systems focus on low energy gamma rays due to practical difficulties in imaging high-energy gamma ray emitters. However, for better resolution and accurate dose delivery calculations in radioimmunotherapy, high-energy gamma rays (¿511 keV) can be highly beneficial [1]. A possible way to image high energy photons to achieve better spatial resolution is available by the so called Compton Cameras [2]. This is possible as Compton cameras are able to provide information on the direction of the incoming Compton scattered photon electronically in contrast to the mechanical apertures used conventionally in SPECTs for the spatial resolution of gamma rays [3]. As the name suggests, these cameras utilize the Compton scattering principle by employing a secondary scattering plane for high energy gammas to interact with. Detection of scattered gamma ray from Compton scattering in an absorber material allows for a reconstruction of the position of the source.

Currently, the biggest challenge in utilizing Compton cameras lies in the simultaneous detection of the scattered electron and photon. Doing so will not only allow for faster reconstruction of the source position but also improve the overall accuracy of the device as well. A possible workaround to this problem is to use Silicon Photomultipliers (SiPMs) coupled with suitable acrylic glass. In principle, the high energy scattered electron should produce Cherenkov radiation as it traverses through the acrylic glass. A simulation of this principle has been done by [4] and [5], which show promising results.

The choice to use SiPMs over the conventionally used Photomultiplier Tubes (PMTs) is because SiPMs not only offer a higher gain (factor) than PMTs, able to achieve subnanosecond timing resolution, capable of operating at a much lower high voltage but they are also much more smaller in size than PMTs. Utilizing these characteristics, the project aims to move beyond the physical limitations of PMTs and improve the overall spatial resolution of nuclear imaging devices in general and Compton cameras in specific. Further applications of the project include monitoring of dose delivery during radiation therapy as well as being able to identify various radioisotopes by coupling with Compton cameras. Other potential applications of the include being able to detect and monitor radiation hotspots with Compton cameras [6] as well as possible homeland security applications.

The aim of this thesis is to detect Cherenkov radiation emitted by electrons traversing through an acrylic glass with a beta source to simulate high energy scattered electrons. This thesis will also take an introductory glance at the analysis of the circle generated from the detected Cherenkov cone on the SiPM by using automated computer vision algorithms, namely the Circular Hough Transform. Chapter 2 concludes after a theoretical description of Compton Camera, SiPMs, and the Cherenkov Effect. The following chapter deals with the Circular Hough Transform and its application in Matlab for the detection of the circle of the Cherenkov cone. Chapter 4 addresses the experimental setup along with the electronics used for coincidence detection of photons through the SiPM. Chapter 5 discusses the obtained results and the last chapter concludes with the summary and implication of the obtained results in providing a proof of principle for the detection of Cherenkov radiation via SiPMs and their application in the enhancement of Compton Camera.

Chapter 2

Theoretical Background

In this chapter, the theoretical background of Compton Camera, Cherenkov Radiation and SiPMs are discussed. If the reader is familiar with these concepts already, it is recommended to skip this chapter.

2.1 Photon's Interaction with Matter

A beam of photons, at lower energies, is not degraded in energy when it traverses through a piece of matter but only sees reduction in its intensity. This is due to the fact that the main three interactions of the photon with matter remove photons from the beam entirely either due to scattering or absorption. The photons collected at the end are those which went through the material without any interaction and as a result, are those which retain their original energy. Due to the small cross section and lack of electrical charge, photons are many times more penetrating than charged particles. Including also higher energies, photons mainly interact with matter in three ways:

- Photoelectric Effect
- Compton Scattering
- Pair Production

The interactions are shown in Figure 2.1, where the cross section of the interactions is plotted as a function of the energy of the photon beam. As evident from the figure, for low energy values, photoelectric effect is more probable while for very high energy values pair production becomes the dominant effect. The absolute cross sections change for different materials but the energy range where certain interactions dominate are more or less the same. Here we will only discuss the Photoelectric effect and Compton Scattering as the energy range for Pair Production is outside the scope of this thesis.

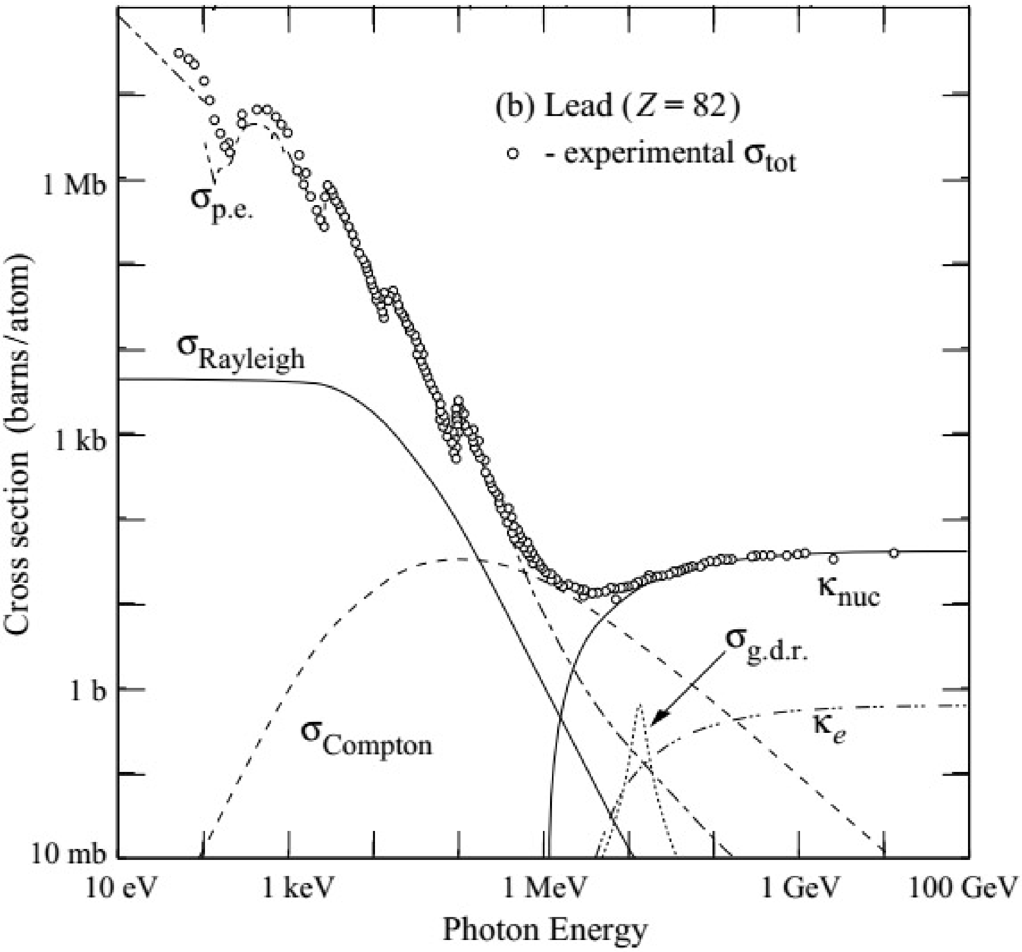

Figure 2.1: Photon's total cross section as a function of energy in Lead [7]. Where:

$$\begin{aligned}\sigma_{\text{p.e.}} &= \text{Atomic photoelectric effect}\\ \sigma_{\text{Rayleigh}} &= \text{Rayleigh (coherent) scattering}\\ \sigma_{\text{compton}} &= \text{Compton (incoherent) scattering}\\ \kappa_{\text{nuc}} &= \text{Pair production, nuclear field}\\ \kappa_{\text{e}} &= \text{Pair production, electron field}\end{aligned}$$

2.1.1 Photoelectric Effect

This process involves the absorption of the energy of a photon completely by an atomic electron, knocking it out of its shell. Due to momentum conversation, this process is not possible for free electrons but requires bound electrons with the atomic nucleus being the third collision partner. The energy of the outgoing electron is given by:

$$E = h\nu - B.E. \tag{2.1}$$

where B.E. is the binding energy of the electron. The cross section as a function of the incident photon energy is shown in Figure 2.2. The cross section essentially gives us a probability for the process to occur. As it can be seen, the cross section decreases with increasing energy of the photons. At certain energies, it increases rapidly when the binding energy for electrons in an a certain atomic shell is reached. This sharp increase is known as the K-absorption edge. Similarly, we also have L-absorption edge, M-absorption edge, etc.

The total cross section for photoelectric effect in the non relativistic range is given by the Born approximation for the K shell as [9]:

$$\sigma^K_{photo} = \left(\frac{32}{\epsilon^7}\right)^{(1/2)} \alpha^4\, Z^5\, \sigma_e^{Th}\ \mathrm{cm}^2/\mathrm{atom} \tag{2.2}$$

where $\epsilon = E_\gamma / m_e c^2$ is the reduced photon energy and σ_e^{Th} is the Thomson cross section for elastic scattering of photons on electrons. For energies which are higher ($\epsilon >> 1$), the photoelectric effect is given as [9]:

$$\sigma_K^{photo} = 4\pi r_e^2 Z^5 \alpha^4 \frac{1}{\epsilon} \tag{2.3}$$

The cross section depends on the atomic number Z. This dependence varies with the photon energy and in MeV range it goes as Z to the 4th or 5th power as the photon doesn't interact directly with isolated electrons. Z dependent corrections to equation 2.3, make σ_K^{photo} a more complicated function of Z. This is an important aspect to consider while choosing materials for γ-ray detectors as higher Z materials provide a bigger cross section and have lower scattering lengths.

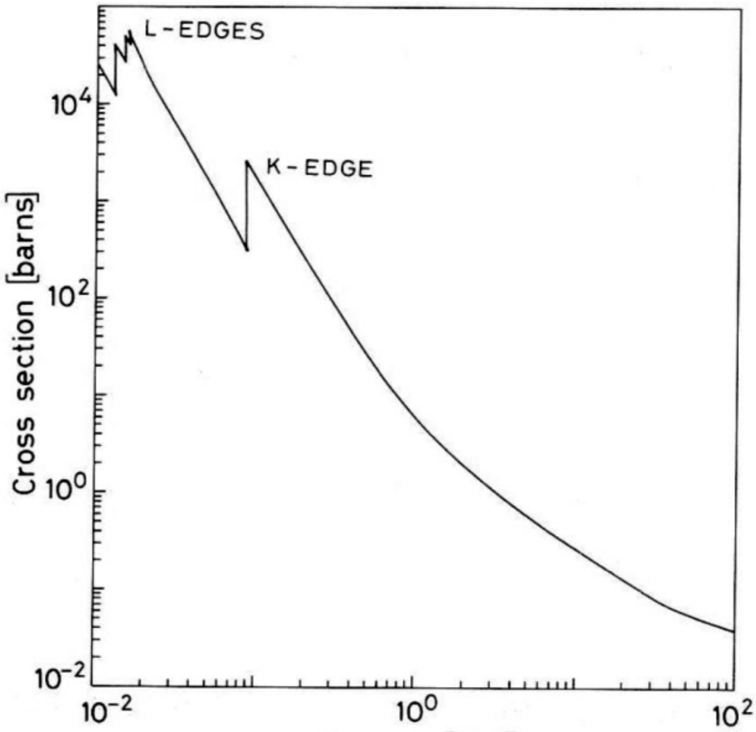

Figure 2.2: Photoelectric cross section for Lead [8]

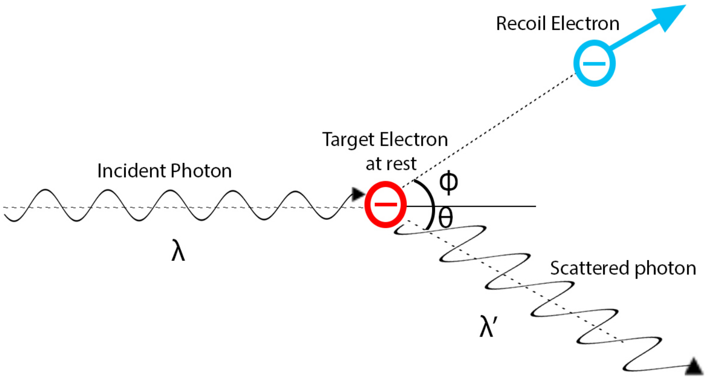

Figure 2.3: Compton Scattering
labelfig:2.3

2.1.2 Compton Scattering

Compton Scattering is amongst the most recognized and understood process for inelastic scattering for photon interaction with matter. It is the process in which photons scatter off of free electrons. In matter, electrons are bound but if the energy of the coincident photon is high enough, the binding energy can be neglected and electrons can essentially be treated as free.

In the process of compton scattering, a photon is incident on an atom, as shown in figure 2.2. The photon transfers some of its energy to the electron, knocking it out of its shell. As this is an inelastic scattering, the wavelength of the incident photon changes, which can be calculated by using the equation:

$$\lambda^{'} - \lambda = \frac{h}{m_e c}(1 - \cos\theta) \tag{2.4}$$

Where λ and $\lambda^{'}$ are the wavelengths of the incident and scattered photon respectively, h is the planck's constant, m_e is the mass of electron at rest, c is the speed of light and θ is the angle of the scattered photon.

Applying energy and momentum conservation, we can also obtain a relation between the scattering angles of the photon and electron, which is stated below

$$\cot\phi = (1 + \gamma)\tan\frac{\theta}{2} \tag{2.5}$$

where $\gamma = h\nu/m_e c^2$ and $h\nu$ is the energy of the incident photon.

2.2 Charged Particle's Interaction with Matter

Interactions of charged particles passing through matter are mainly governed by inelastic collisions of the particles with the atomic electrons in the material and elastic scattering from the nucleus of the atoms. Although these effects are dominant and can occur multiple times per unit path length of the particle trajectory through the matter, there are other processes such as emission of

Cherenkov radiation, bremstrahlung and nuclear reactions that can occur as well. Out of the aforementioned interactions, only the emission of Cherenkov radiation is of importance to us as the other processes are extremely rare (out of all scatterings, 90% are small energy losses, up to 100 eV, occurring due to multiple scattering [7]) by comparison.

2.2.1 Multiple Scattering

Multiple scattering refers to the Coulombic interaction of the charged particle with electrons and nuclei. These processes cause a very slight deflection from the original path of the charged particle. The angular distribution of the deviations which occur by multiple Coulomb scattering are described by *Molière's theory.* It is a Gaussian distribution centered around 0 for small scattering, with a slight tail indicating the probability of larger scattering angles which are caused by collisions of the charged particles with the nuclei, as shown in figure 2.3. The root mean square of the scattering angle distribution is given by [7]:

$$\Theta_{rms}^{proj.} = \sqrt{< \Theta^2 >} = \frac{13.6\ MeV}{\beta\ c\ p}\ z\ \sqrt{\frac{x}{X_0}}\,[1 + 0.038\ \ln(x/X_0)] \tag{2.6}$$

where p (MeV/c) is the momentum, $\beta{\cdot}c$ is the velocity, z is the charge of the scattered particle and x/X_0 is the thickness of the scattering medium, measured in units of radiation length (defined below).

Radiation Length

It is the distance over which the electron energy is reduced due to bremsstrahlung only by a factor of 1/e. Usually, radiation length is measured in g/cm^2. Most materials have this value experimentally calculated and already tabulated [11] but a rough approximation can also be done for any material provided the atomic number Z and mass A of the material are known, by using [8]:

$$X_0 = \frac{716.4\ (\mathrm{g/cm^2})\ A}{Z(Z+1)\ \ln(287/\sqrt{Z})} \tag{2.7}$$

The calculated values are accurate to within 2.5% except for Helium, where the error rises to 5%. For compounds and materials, this quantity can be calculated by using Bragg's rule [8]:

$$\frac{1}{X_0} = \sum \frac{w_j}{X_j} \tag{2.8}$$

Where w_j and X_j are the fraction by weight of the jth element in the mixture and radiation length for the jth element respectively.

Differential Cross Sections

For finding and simulating the interaction of the electron path through a material, it is important to say a few notes and have a mathematical formalism to calculate the differential cross sections for it's interaction with the material. Differential scattering cross section refers to the differential ratio between the

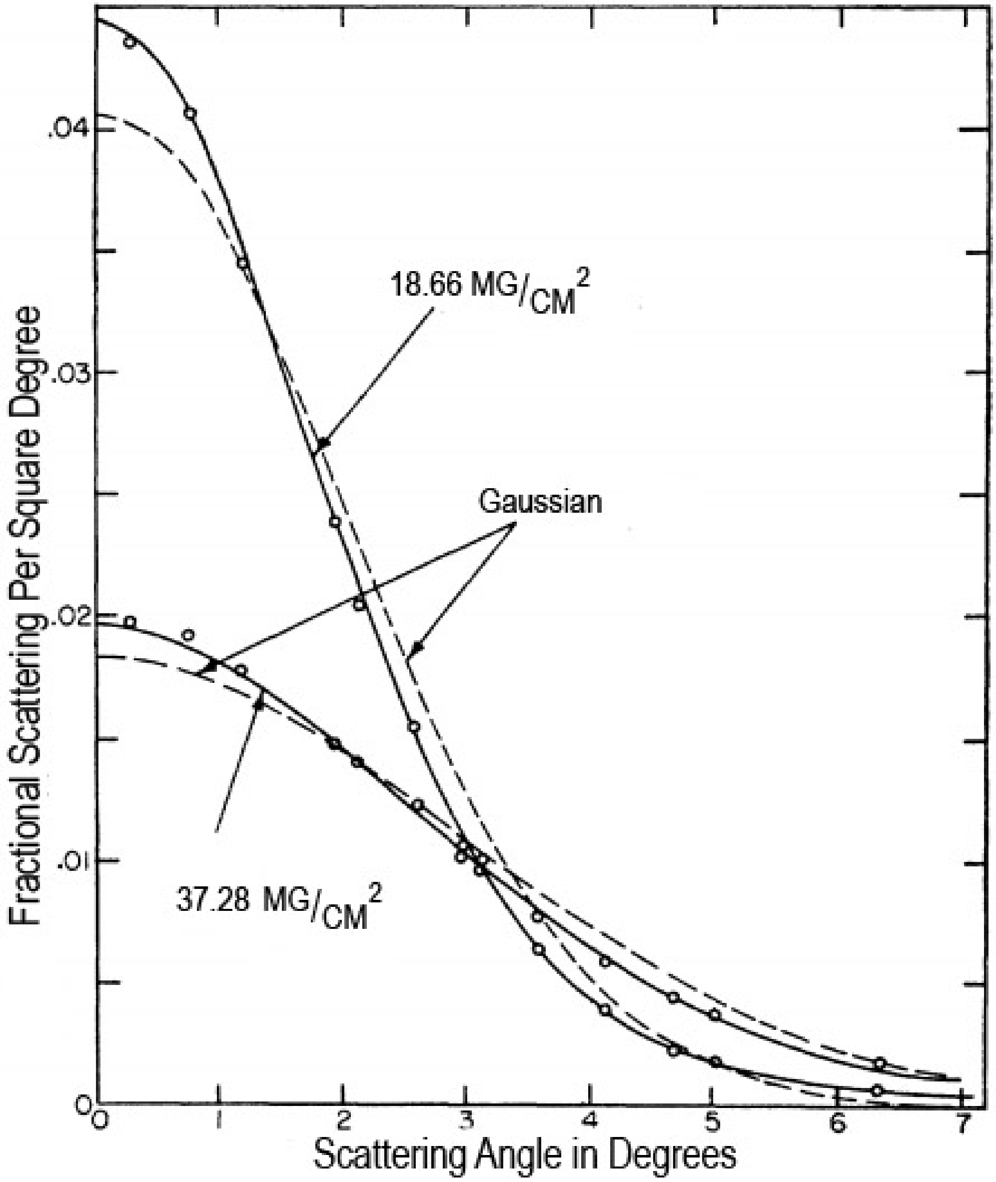

Figure 2.4: Angular Distribution of electrons, having energy of 15.7 MeV, scattered from a thin gold foil. Experimental values (dots) are fitted with Molière's theory (solid) and compared to a Gaussian approximation (dashed) [10].

infinitesimal area $d\sigma$ and the corresponding solid angle $d\Omega$ on which the particle will scatter. The total cross section is the result of the integration over all scattering angles and processes.

As previously mentioned, the electron on some occasions interacts with the nuclei and is deflected at large angles. The elastic cross section (cross section for elastic scattering) the particles undergoes is given by Rutherford Scattering, as stated below:

$$\frac{d\sigma}{d\Omega} = \frac{\sigma_0(pv)}{\sin^4\left(\dfrac{\theta}{2}\right)} \tag{2.9}$$

where

$$\sigma_0 = \frac{z\ Z\ e^2}{2\ p\ c\ \beta} \tag{2.10}$$

and θ is the scattering angle, Z is the atomic number of the scattering material, and e is the electron's elementary charge.

However, most of the electron's interactions are the Colombic small angle scattering, whose differential cross section was famously given by Molière's as [12] (or in English: [13] and [14]):

$$\frac{d\sigma}{d\theta} = 32\pi\sigma_0 \frac{\theta}{(\theta^2 + \theta_a^2)^2} \tag{2.11}$$

where, θ_a is the screening angle which is a modification needed since the electrons limit the small angle range. If this correction is not made, the total cross section will be infinite. The screening angle is mathematically calculated as:

$$\theta_a = \theta_0\sqrt{1.13 + 3.76a^2} \tag{2.12}$$

with $a = \dfrac{zZ}{137\beta}$ and $\theta_0 = \dfrac{\lambdabar}{a_{TF}}$, $\lambdabar$ is the De Brogli wavelength and a_{TF} the Thomas Fermi radius.

The two cross sections, for small and large angle scattering, are generally divided by an angle θ_g, chosen in such a way that we get a smooth function. For small angle scattering, the scattering angle's range is taken as:

$$\theta \in [0\ ;\ \theta_g] \tag{2.13}$$

and for large angles, the scattering angle is taken from:

$$\theta \in [\theta_g\ ;\ \pi] \tag{2.14}$$

2.2.2 Cherenkov Radiation

Cherenkov radiation is emitted when the speed of a charged particle, traveling through a dielectric medium, is greater than the speed of light in the same medium. Mathematically, this can be expressed as:

$$v_{particle} > c/n \tag{2.15}$$

Where n is the refractive index of the medium. As long as the speed of particle is greater than the ratio c/n, we will see an electromagnetic shock wave, similar to a sonic shock wave (commonly referred to as a sonic boom). The angle of the conical wavefront, as shown in figure 2.4, can be calculated by using:

$$\cos\theta_c = \frac{1}{\beta n(\omega)} \tag{2.16}$$

Here we should note that the angle is dependent on the speed of the particle as well as the frequency ω of the emitted radiation. Consequently, we can also calculate the number of photons produced per unit path length and frequency of a particle as well by using the equation:

$$\frac{d^2N}{d\omega dx} = \frac{z^2\alpha}{c}\sin^2\theta_c \tag{2.17}$$

Where after substituting the value of θ_c, we get

$$\frac{d^2N}{d\omega dx} = \frac{z^2\alpha}{c}\left(1 - \frac{1}{\beta^2 n^2(\omega)}\right) \tag{2.18}$$

where z is the charge of the particle, α is the fine structure constant given by $\alpha = \left(\frac{e^2}{4\pi\epsilon_0\hbar c}\right) \approx \frac{1}{137}$, and N is the number of photons emitted. In terms of wavelength, this relation can be given as:

$$\frac{d^2N}{d\lambda dx} = \frac{2\pi\alpha z^2}{\lambda^2}\left(1 - \frac{1}{\beta^2 n^2(\lambda)}\right) \tag{2.19}$$

From this equation, one can see that the emission per wavelength increases with decreasing wavelength as shown in figure 2.6. This equation also helps us to determine the amount of photons emitted per length in a specific wavelength range by integrating it over λ. This gives us:

$$\frac{dN}{dx} = 2\pi z^2\alpha\sin^2\theta_c\int_{\lambda_1}^{\lambda_2}\frac{d\lambda}{\lambda^2} \tag{2.20}$$

Here λ_1 and λ_2 are the wavelength of interest. Since the relation depends on the wavelength inversely, we need to work with Silicon Photomultipliers (discussed

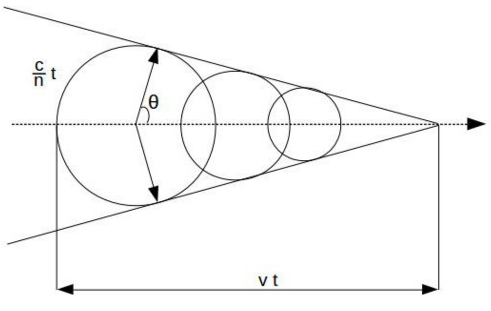

Figure 2.5: Cherenkov Radiation

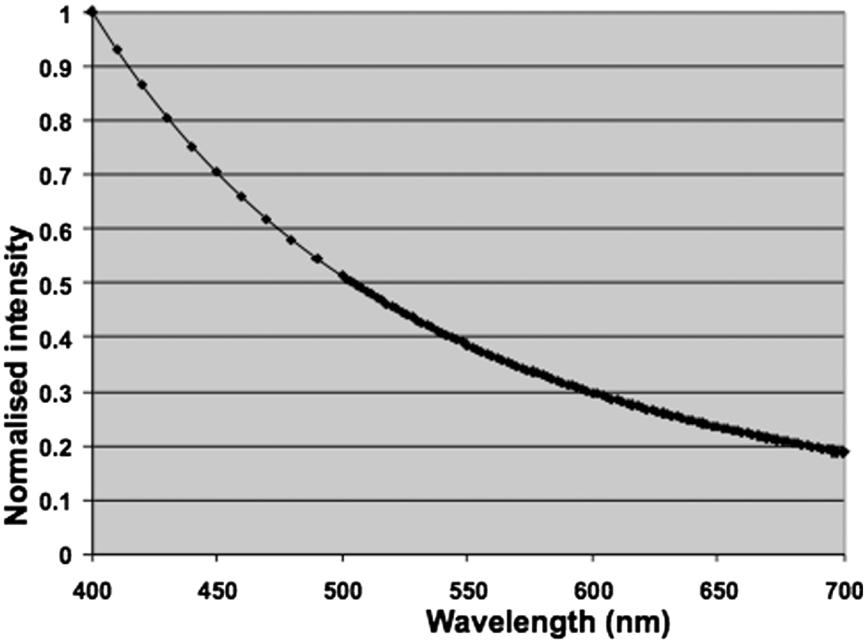

Figure 2.6: Normalized intensity vs. wavelength for Cherenkov radiation emission in the range of 400 to 700 nm [15]

in section 2.4) which have a higher photo-detection efficiency in near UV range to detect the maximum number of photons. The number of the emitted photons is proportional to the path length of the charge particle, as long as the energy of the particle is above the Cherenkov threshold. Therefore, the number of Cherenkov photons increases with the initial energy fo the charged particle.

2.3 Compton Camera

A Compton Camera is a gamma ray detector that utilizes the concept of Compton scattering to build images without the use of any mechanical collimators. The camera allows for reconstruction of the origin of a photon source on the surface of a "Compton Cone".

2.3.1 Working Principle

The basic working principle of the camera is shown in figure 2.7. The camera consists of two radiation detectors, namely the scatterer and absorption detector, working in coincidence. When a gamma particle hits the scattering plane, it goes through Compton scattering, producing an electron along with the scattered photon. The photon is then detected via photoelectric absorption at the second detector (absorber plane), which constitutes as a single coincidence event. The detected photon is then backtracked to form a Compton cone. The resulting Compton scattering angle, represented by θ can easily be calculated by using the formula:

$$\cos\theta = 1 - m_e c^2 \left(\frac{1}{E_\gamma - E_S} - \frac{1}{E_\gamma} \right) \tag{2.21}$$

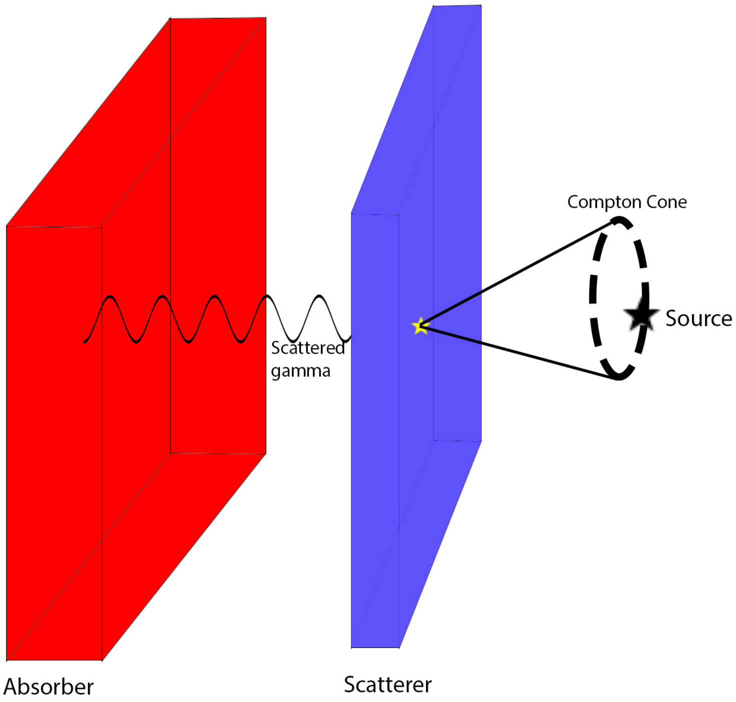

Figure 2.7: Block Diagram showing the working principle of a Compton Camera: The scattered gamma from the scatterer is traced back to it's original Compton cone and the location of source is found by the intersection of multiple Compton cones.

Here m_0 is the rest mass of an electron, E_γ is the incident gamma energy and E_S is the energy deposited in the scatterer plane during Compton scattering. In such a way, using multiple coincidence events, we get a plethora of cones. The intersection of these cones at a common point allows us to draw a conclusion on the initial position of our source.

2.3.2 Advantages

Thanks to the increased sensitivity of the Compton Camera compared to conventional SPECTs, they have a high potential for use in nuclear medicine application [16]. The camera can not only provide better images in terms of position and energy resolution, with an improved signal to noise ratio, and shorter counting times but it can also reduce the radioactive dose a patient has to receive during the imaging process [17]. Also, as the camera does not use any mechanical collimation, it opens the door for imaging with multiple radiotracers having different energies simultaneously [18].

2.3.3 Shortcomings of Compton Cameras

One of the most major challenges Compton Cameras faces is the simultaneous detection of both the scattered electron and photon. This can be corrected by finding a method to reduce the effects of parallax from incident gamma rays which are inclined as well as reducing the disbursed energy deposition due to multiple Compton interactions. This obviates the cameras from providing better spatial resolution than they are capable of as it has an adverse effect on the reconstruction of the gamma-ray track based on kinematic considerations.

Multiple solutions have been suggested to tackle these challenges. One of these approaches is the one mentioned in the Monte Carlo study done in [5], which attempts to use the detection of Cherenkov Radiation for the detection of the scattered electron and employ it for an accurate and faster reconstruction of the position of the source.

Usage of Silicon Photomultipliers over Photomultipler Tubes

Since we are interested in reducing the effects of parallax for inclined photon incidence as well as the dispersed energy deposition on the detector due to multiple Compton scattering events, we need some optical imaging involving 3D reconstruction of secondary tracks. This is where the detection of Cherenkov photons is proposed to be employed to increase the timing resolution of the signal as well as reduce the need of finding expensive scintillator materials and opening up choices for easily available materials (PMMA, glass, water) [5].

Since the wavelength of Cherenkov photons is in the near UV range, we are interested in using devices which offer better detection in that wavelength range. The recent developments in Silicon Photomultiplier (SiPM) technology have made them one of the prime candidates for this purpose [19]. SiPMs are able to work in the UV range at a significantly lower operating voltage, provide a better spectral sensitivity, are not affected by magnetic fields, and most importantly have single photon timing resolution which is much smaller (in the range of ps) than a PMT [20]. All of the aforementioned characteristics and the relatively small size of a SiPM (compared to a PMT), makes them ideal for the use of detection of Cherenkov photons.

2.4 Silicon Photomultipliers

2.4.1 Photodiodes

Photodiodes are semiconductor devices that have a PN or PIN structure, which are capable of detecting photons by utilizing the photoelectric effect. Stated briefly, a PN structure refers to a P-N junction which is made by combining two extrinsic semiconductors already doped with trivalent (P-type) and pentavalent (N-type) impurities. Whereas a PIN structure refers to a p-n junction that has an intrinsic semiconductor in the region between the p and n-type. Whenever a photon is incident on the diode, an electron-hole pair is generated, provided the photon had sufficient energy. The electron-hole pair is then separated with the help of an external voltage, producing a photocurrent in the diode.

Photodiodes usually operate in reverse bias mode to expand the inherent depletion region in the device. This also increases the electric field. For a normal p-n junction photodiode, the electron hole pairs are produced when a photon with sufficient energy, that is greater than the bandgap of the semiconductor(for Si it is about 1.11 eV [21]), strikes the p-, n- or the depletion region. However, electron-hole pairs which are generated further away from the depletion region make no contribution to the photocurrent, as they recombine shortly after generation. Only the pairs which are within the diffusion length of the depletion region or in the region itself make electron-hole pairs. These pairs are then separated by the electric field to make a contribution to the signal by drifting towards their respective electrodes and generating a drift current. The signal produced is proportional to the number of photons incident on the diode.

A PIN photodiode, as shown in Figure 2.8, differs from a p-n junction by an inclusion of an high ohmic intrinsic semiconductor sandwiched between two heavily doped p and n junctions. This configuration increases the overall photosensitive area of the photodiode by increasing the depletion region, which generates the drift current producing electron-hole pairs. This results in a higher quantum efficiency (QE) than a normal p-n photodiode. As both of these devices don't utilize any sort of internal amplification, they can only be used with relatively high fluxes of about 200 photoelectrons or more [22].

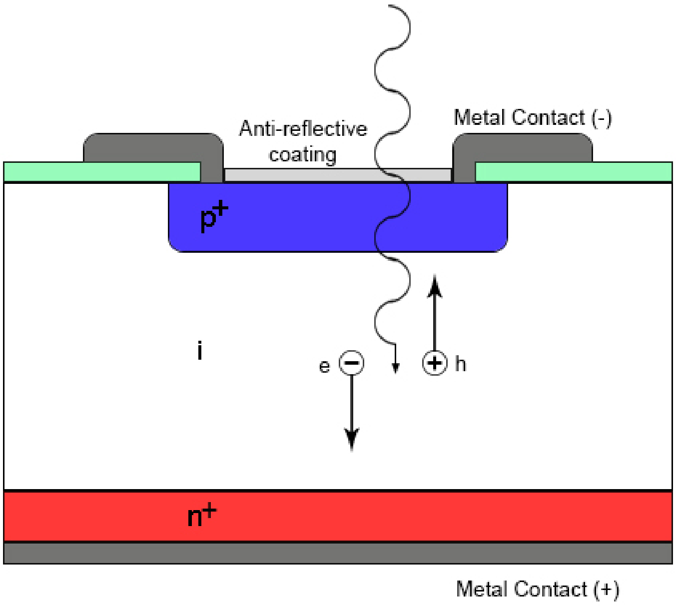

Figure 2.8: Block diagram representation of the PIN photodiode. Bias voltage is applied from the indicated metal contacts. The electron-hole generation and separation process in the intrinsic semiconductor layer is shown. Adapted from [23]

2.4.2 Avalanche Photodiodes (APDs)

Avalanche Photodiodes have a p-n junction which is operated in reverse bias mode and utilize the same detection principle as PIN photodiodes. An incoming photon creates electron-hole pairs by photoelectric effect, which are then separated by the applied electric field. Due to a high value of the applied bias voltage, the electron or hole is accelerated strongly enough in between collisions to obtain sufficient energy to create an avalanche process of creation of new electron-hole pairs (impact ionization). This results in an amplified current and acts as an internal signal amplification, making the device useful for lower intensity light detection.

By adjusting the applied bias voltage, within a certain range, the gain of the device can be controlled. However, exceeding the breakdown voltage can lead to an exponential increase of the generated photocurrent by the production of additional electron-hole pairs created by holes. This in turn can have a negative impact on the device and should be prevented by adjusting the applied reverse bias carefully.

A typical avalanche photodiode is shown in Figure 2.9. The photodiode consists of an absorption region where incident photons generate the electron-hole pairs. The generated electrons are then drifted towards the multiplication region, where a high electric field for the avalanche process is provided. This construction provides a safe performance by keeping the multiplication of electron-hole pairs generated by holes to a minimum. These devices are sensitive to intensities of about 10 photoelectrons [22].

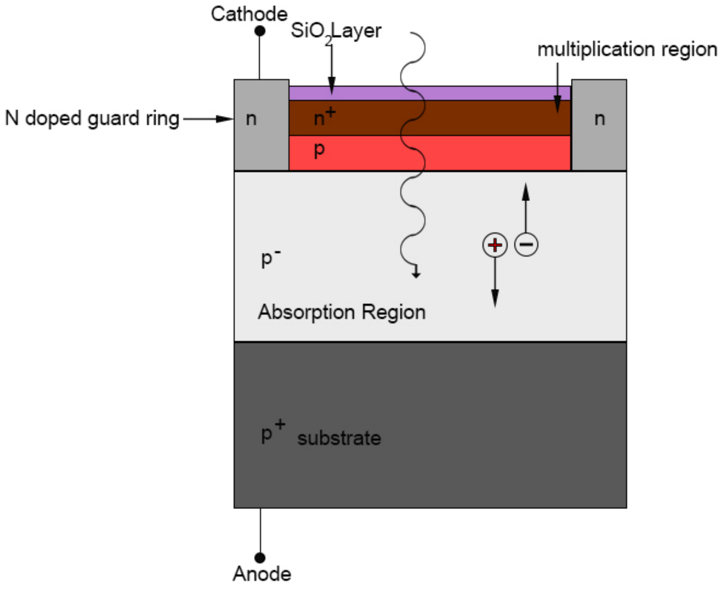

Figure 2.9: Block diagram representation of an Avalanche Photodiode. Adapted from [24]

2.4.3 Geiger Mode APDs

These devices are an advancement of avalanche photodiodes. They are constructed to work beyond the break down point of the APD, where we can extract charge carriers faster than the time it takes for impact ionization to stop completely. As a result we get an exponential increase in charge carriers with time, rather than the linear relation we had with APDs. Due to similarity of the device's operation to a Geiger-counter, these devices are called Geiger-mode APDs (GAPDs) or Single Photon Avalanche Photodiodes (SPADs).

After a certain voltage, the number of charge carriers generated by the impact of a photon increases exponentially with time. This condition is referred to as "avalanche breakdown" and the voltage after which this process begins is called the "breakdown voltage" of the diode. The growth of photocurrent is limited by the diodes's internal resistance, which means that the current does not keep growing. As the current increases, the voltage drops till it drops to V_{bd} at which a steady rate of ionization and extraction is reached. An external large resistance (up to 10MΩ), connected in series, is used to shut off the avalanche current. This process is called passive quenching of the signal and the resistance is referred to as the quenching resistor, denoted as R_Q. Alternatively, electronics can also be used instead of a resistor to quench the signal, which is referred to as active quenching. By quenching the avalanche, the diode is able to recharge and detect further photons.

Even though the gain of a SPAD is finite, it is still more than what we get from the linear relation from a normal APD, as shown in figure 2.10, which is why these devices can be used for the detection of a single photon. Mathematically,

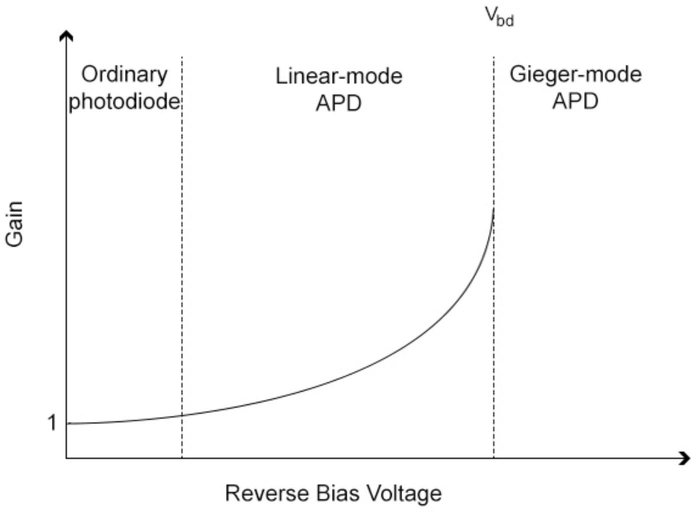

Figure 2.10: Schematic drawing showing reverse bias voltage versus gain of photodiodes. Above breakdown voltage (V_{bd}), the gain becomes virtually infinite. Adapted from [25]

the gain of a SPAD is given by [26]:

$$G = \frac{Q}{e} = \frac{C_D.\Delta V}{e} \simeq 10^6 \tag{2.22}$$

where C_D is the preavalanche capacitance of the photodiode and ΔV is the overvoltage that is defined as:

$$\Delta V = |V_{Bias} - V_{bd}| \tag{2.23}$$

2.4.4 Silicon Photomultipliers (SiPMs)

A Silicon Photomultiplier (SiPM), also known as Multi-Pixel Photon Counter or MPPC, is a pixelated detector that typically consists of several thousand single SPADs connected in parallel and a quenching resistor. Each SPAD in a SiPM is called a pixel or a microcell and has a pixel pitch in the order of 10-100 μm. The overall active areas for SiPMs range from 1 mm^2 to 6 mm^2 and they have spectral sensitivity in the UV to IR range.

Each pixel in a SiPM is made to operate above their breakdown voltage in Geiger mode. To minimize optical crosstalk (discussed ahead), the microcells are separated by opaque trenches. The trenches, electrical circuits and resistors reduce the effective sensitive area of SiPM. The area in which photons are detected is called geometric efficiency or fill factor.

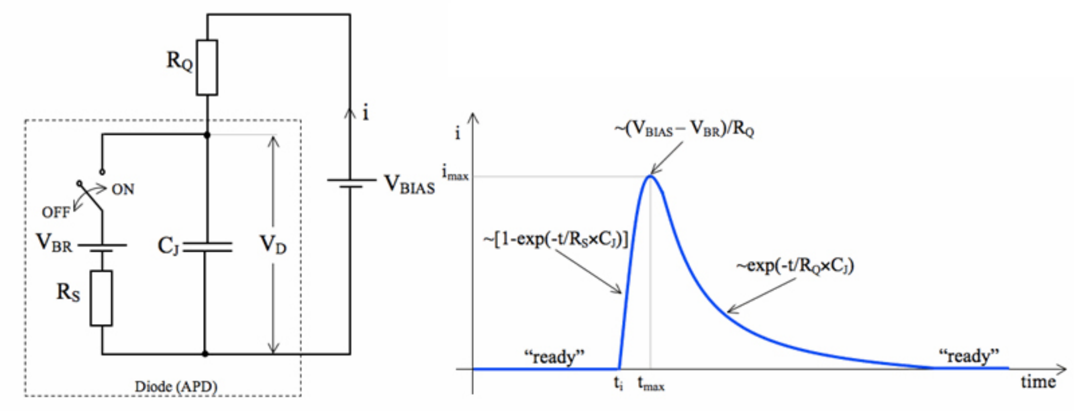

Figure 2.11: A circuit diagram with the resultant waveform after a photon impinges on the SiPM. Image taken from [27]

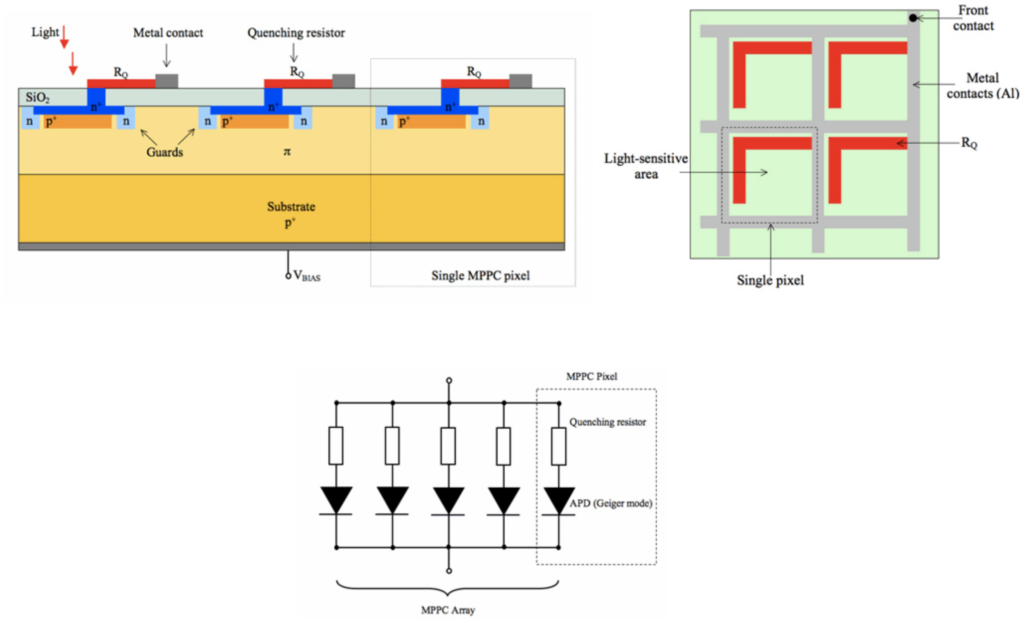

Figure 2.12: Schematic drawing showing the typical structure of a SiPM. From left to right: a cross section of three microcells, top view of the SiPM, equivalent electrical circuit. Please note that this is just a representation of the SiPM for getting acquainted with the technology and does not accurately depict the newest generation of the SiPM [20]

Gain

A typical waveform obtained after a photon is incident on the SiPM is shown in figure 2.11. In the absence of light, the switch S remains open and the voltage on junction capacitance C_j is the applied bias voltage. After a photon hits the SiPM and triggers an avalanche, S closes and C_J begins to discharge through R_s causing a voltage drop in the quenching resistor R_Q, resulting in current flowing through the electrodes of the SiPM.

The gain of the SiPM can be given as [27]:

$$G \approx \frac{\Delta V . C_J}{e} = \frac{Q_{1pe}}{e} \tag{2.24}$$

Where Q_{1pe} corresponds to the charge created by one avalanche or 1 photon equivalent peak.

An important thing to note is that V_{br} depends on temperature as shown in [28] and [29]. Therefore to eliminate the indirect dependence of gain on temperature, the SiPM should be operated at a constant ΔV. As evident from equation 2.24, there is a linear relation between the overvoltage and gain of a SiPM.

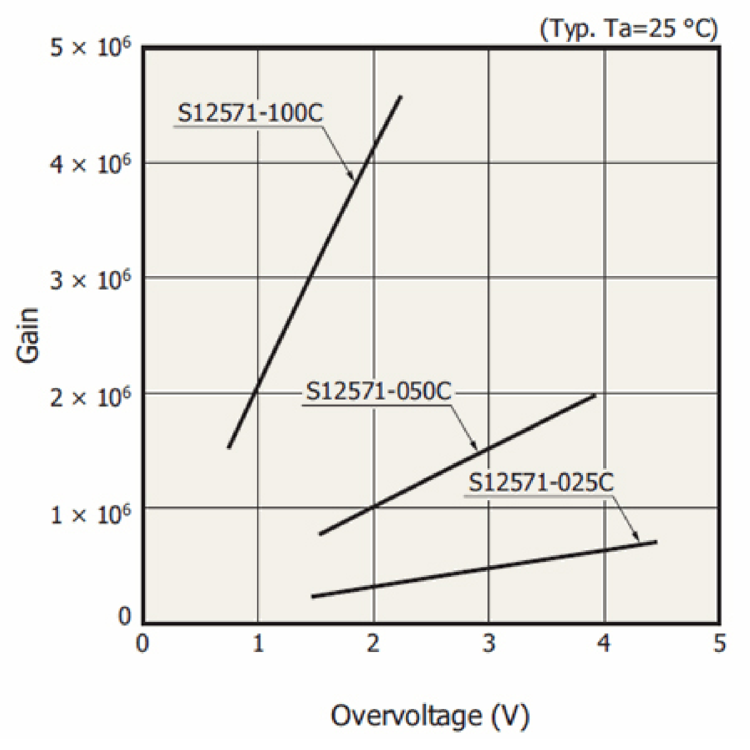

Figure 2.13: The linear dependence of gain on overvoltage for different SiPMs made by Hamamatsu [20]

Crosstalk

Crosstalk refers to the process which occurs when a primary discharge triggers secondary discharges in one or more neighboring pixels. On average about 30 photons per typical avalanche are generated by electrons that contribute to an avalanche in Silicon [30]. The photons generated in such a way may be absorbed within (a) the pixel it was generated in, (b) the non photosensitive area of the SiPM, or (c) a neighboring pixel that may give rise to secondary discharges. The secondary discharges in neighboring channels (case c) create new avalanches that give additional signals and add to the signal peak. Due to this, an output signal which is higher than the amount of incident light on the SiPM is obtained as shown in figure 2.14.

To reduce this effect, manufacturers use trenches which are filled with optically opaque materials. This reduces the probability of crosstalk but also has a negative impact on the overall photon detection efficiency by decreasing the geometrical efficiency of the device.

Afterpulses

Another thing shown in figure 2.14 are the “Afterpulses”. These are generated when a secondary avalanche is formed in a pixel that is still recovering. They occur after some time of the primary avalanche due to release of trapped charges that are present due to the impurities in the Silicon used for the SiPM. The amount of charge generated by afterpulses is directly proportional to ΔV due to the stronger electric field. Technically, these afterpulses can also be generated after a pixel has recovered but then we can’t differentiate them from real photon peaks.

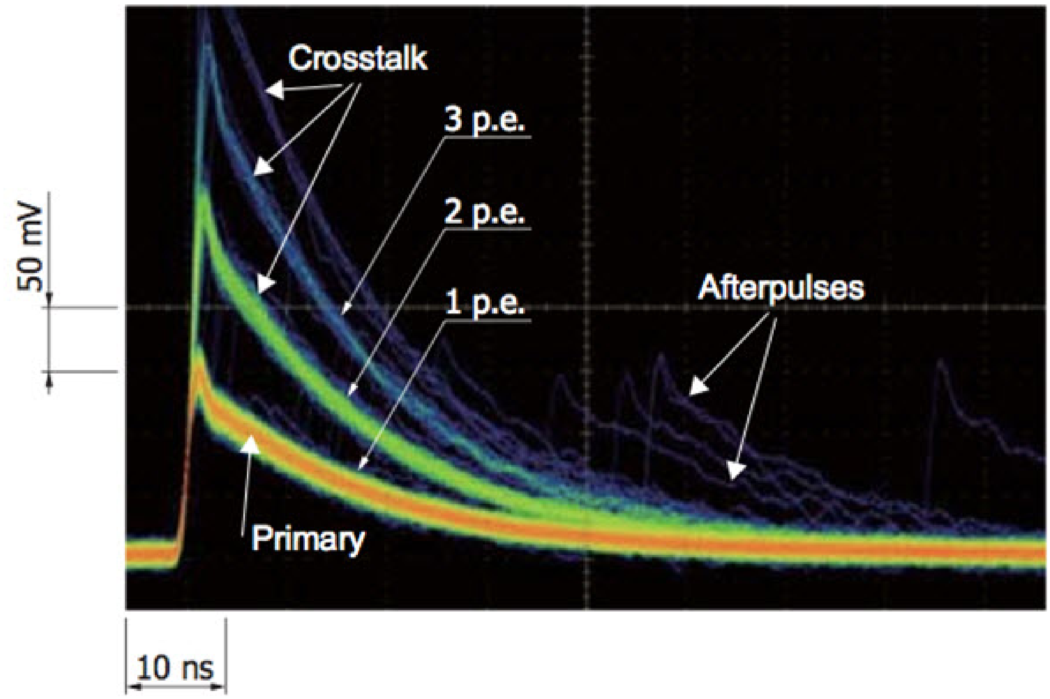

Figure 2.14: 1 p.e. shows the 1 photon equivalent peak which is present in the absence of crosstalk. Higher peaks correspond to the number of crosstalk events generated by the primary discharge in the neighboring pixels. The color indicates the frequency of the occurrence of the waveforms, with red being highly frequent and blue consequently being less frequent [20]

Chapter 3

Simulations

In this chapter, the theoretical simulations of small angle scattering as well as the application of Circular Hough Transform for the detection of the radius of Cherenkov cone will be discussed. Before the simulation and their results are discussed, some basic theory will also be touched upon to ensure that the reader is familiar with the concept of Hough Transform.

3.1 Hough Transform

Hough Transform is a method to find different geometrical patterns such as lines, circles, etc. in an image or videos using computers. The method falls under the subject of computer vision, feature extraction to be more specific, and was originally presented for the fast detection of lines in binary images [31] but with time the algorithm was generalized further to include other shapes [32].

3.1.1 Linear Hough Transform

The basic premise of a linear Hough transform is that any point in a binary image can be part of a line. Here, a binary image refers to an image that has only two values, 0 or 1, for all pixels of the image. The algorithm basically takes all non zero pixels in the $(\mathrm{x}\,,\mathrm{y})$ plane of the 2D input image, and treats them as points in a set of possible lines. This is done by parameterizing every point using the parametric line equation ($y = a\,x + b$) and plotting them in parameter space. In the parameter space a line passing through two points can be defined as a connection between origin and a point situated at an intercept b and slope a.

Using the aforementioned logic, a point in the original image is transformed to a plethora of points in the $(\mathrm{a}\,,\mathrm{b})$ plane, which corresponds to all possible lines which can pass through that certain point. A sum over all contributions is taken and as a result the “true line”, the line which was present in the input image i.e. $(\mathrm{x}\,,\mathrm{y})$ plane or the image space, appears as a local maximum in the $(\mathrm{a}\,,\mathrm{b})$ plane. This process is then repeated for all points. The $(\mathrm{a}\,,\mathrm{b})$ plane is referred to as the accumulator plane as it contains the contributions from all points [33].

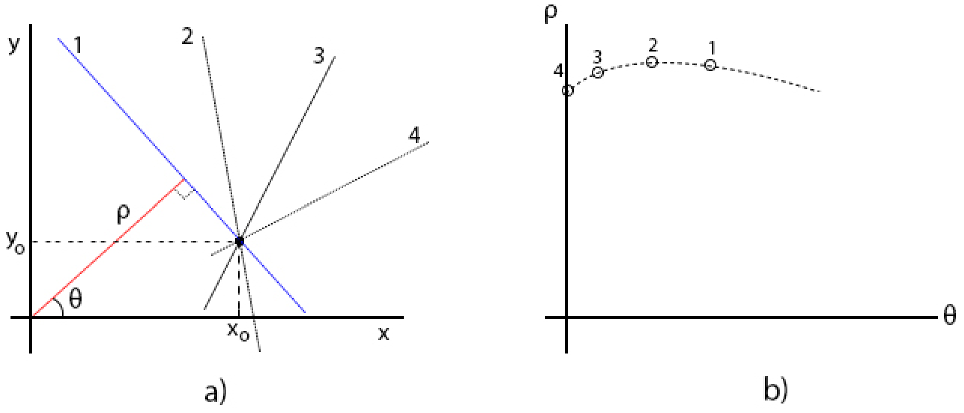

Figure 3.1: A point (x_o, y_o) in image plane can give many lines which are parametrized by ρ and θ (panel a). These parametrized lines when taken together give rise to a characteristic shape in the hough space (panel b). Image adapted from [33]. Note: This is just a graphical representation of the whole process, the characteristic curve for different points is not mathematically accurate.

In practice however, the algorithm varies slightly as it uses polar coordinates because if slope and intercept parametrization is used, vertical lines give unbound values for the slope a. Instead polar coordinates (ρ, θ) are used. Here ρ is the shortest perpendicular distance from the line passing through the point to the origin and θ is the angle ρ makes with the x axis, as shown in figure 3.1. The mathematical form of such parametrization is given by [33]:

$$\rho = x \cos\theta + y \sin\theta \tag{3.1}$$

The plane of (ρ, θ) is called the Hough space. So by using the equation above, points in the (x,y) plane are mapped to a sinusoidal curve in Hough space. A single point where the unique sinusoidal curves of different points intersect each other in the Hough space define a single straight line in the image space. The concurrent curves are stored in the accumulator array along with the rest of the values and the points of intersection act as a local maximum as they have a higher number for their respective bins in the array. This transformation makes the problem of detecting a line in an image transform to a much simpler problem of detecting a point in the Hough space.

Independent of what computer vision software is used, all Hough Transform Line Detection algorithms use a variation of the theory discussed above. Users are able to control the threshold of the local maxima (points in Hough space where the curves intersect with each other) that the program can take as a line. By lowering the threshold, more lines can be detected but some false results can also pop up, which is why a universally set threshold value can't be defined and a certain trade-off has to be made for different images.

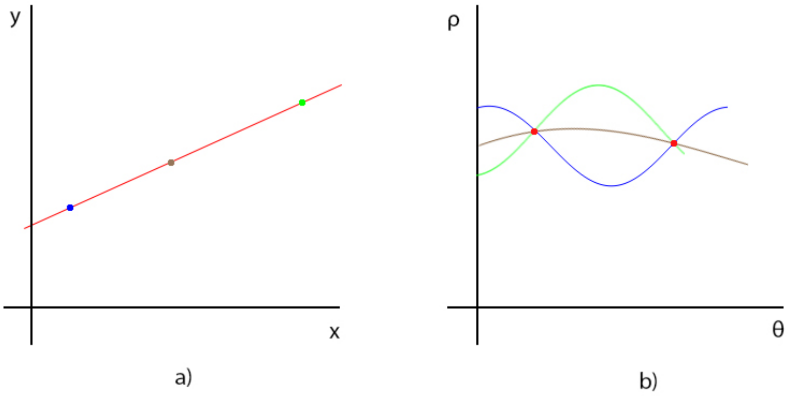

Figure 3.2: The points in line in image space (panel a) give their characteristic curves in the hough space, the points of interaction (panel b) are the maxima in the accumulator array and are detected as the points lying on a line. Note: This is just a graphical representation of the whole process, the characteristic curves are not mathematically accurate.

3.1.2 Circular Hough Transform

In theory, a Circular Hough Transform (CHT) works analogously similar to a linear Hough Transform. However, if the method is translated as is and made to incorporate one additional unknown dimension to the accumulator plane, it would transform to an “accumulator volume” with (x , y) (center point of the circle) and r (radius of the circle) dimensions, which will put an enormous strain on the computer memory and reduce processing speed harshly. This is why different computer vision programs employ certain tricks and voting algorithms to make the process faster.

Known Radius

A simple exercise to reduce processing time is to assume that radius r of a circle is known. The dimension of the accumulator array in terms of unknown quantities goes down and the computer is able to scan 360^o for every non zero pixel by taking it as the center. Mathematically, this is expressed quite simply as:

$$x = a + r\cos(\theta)$$

$$y = b + r\sin(\theta)$$

Where (x , y) represent a point in image space, r is the known radius, θ is the angle and (a , b) are the points in parameter space.

This gives multiple circles in the hough space and the point of intersection of these circles, which are generated from different points, are voted in the accumulator array in hough space. This way the local maxima point towards the actual circle center (x , y) in image space with known radius as shown in figure 3.3.

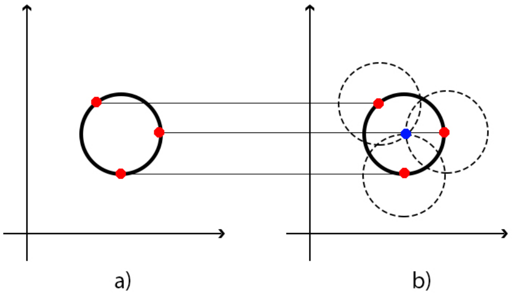

Figure 3.3: The points of the circle in image space (panel a, red dots) is mapped out in hough space with a corresponding circle of known radius r of the original circle (panel b), with the real points as the center. The point of intersection of these circles in hough space (panel b, blue dot) gives the center of the actual circle. Adapted from [34]

Unknown Radius

For circles whose radius is not known, each real point (x , y) which lies on the perimeter of the circle will produce a cone surface in the Hough space, which is in 3 dimensions due to the addition of one more unknown variable. The accumulator array in this case will store intersections points of the cones and give a local maxima at the point where maximum number of cones intersect. This local maxima gives the “true” circle in the image space, as shown in figure 3.4. Another important thing to note is that the size of the accumulator array in the case of unknown radius is equal to values of radii that is looped over, so it is a good practice to provide a certain range of r to decrease processing time.

Figure 3.5 shows a simulated Cherenkov ring detected by a Silicon based detector that has 3 mm PMMA in front of it. The image was generated by

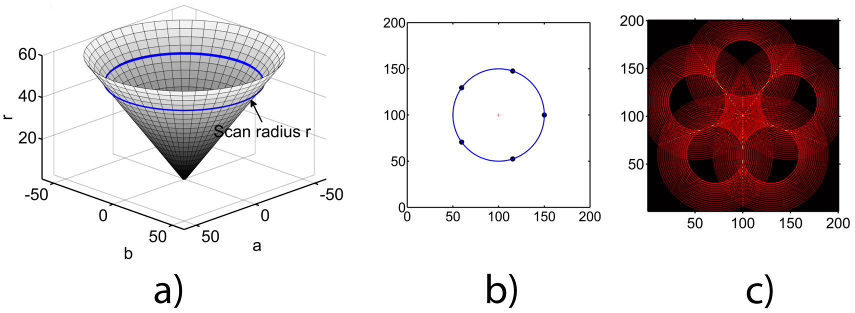

Figure 3.4: A cone is generated (panel a) in the (a, b, r) space and circles are generated for each r for one point in Hough space (panel c). Various cones are generated in the aforementioned method for all corresponding points in image space (panel b) and the point of intersection of these cones in hough space gives the center and radius of the circle. Image taken from [35]

using GAMSIM II [4]. As it is evident a perfect circle is not required for CHT to detect a circle (see section 3.2). We can have a plethora of points generated by a Cherenkov cone and they will still be recognized by the algorithm albeit it may increase the processing time depending upon the resolution of the detector and total number of detected photons. The figure also visualizes the maximum of the accumulator array by drawing it in histogram form as well (panel c). This histogram can be used to get a good approximation of the radius of the circle.

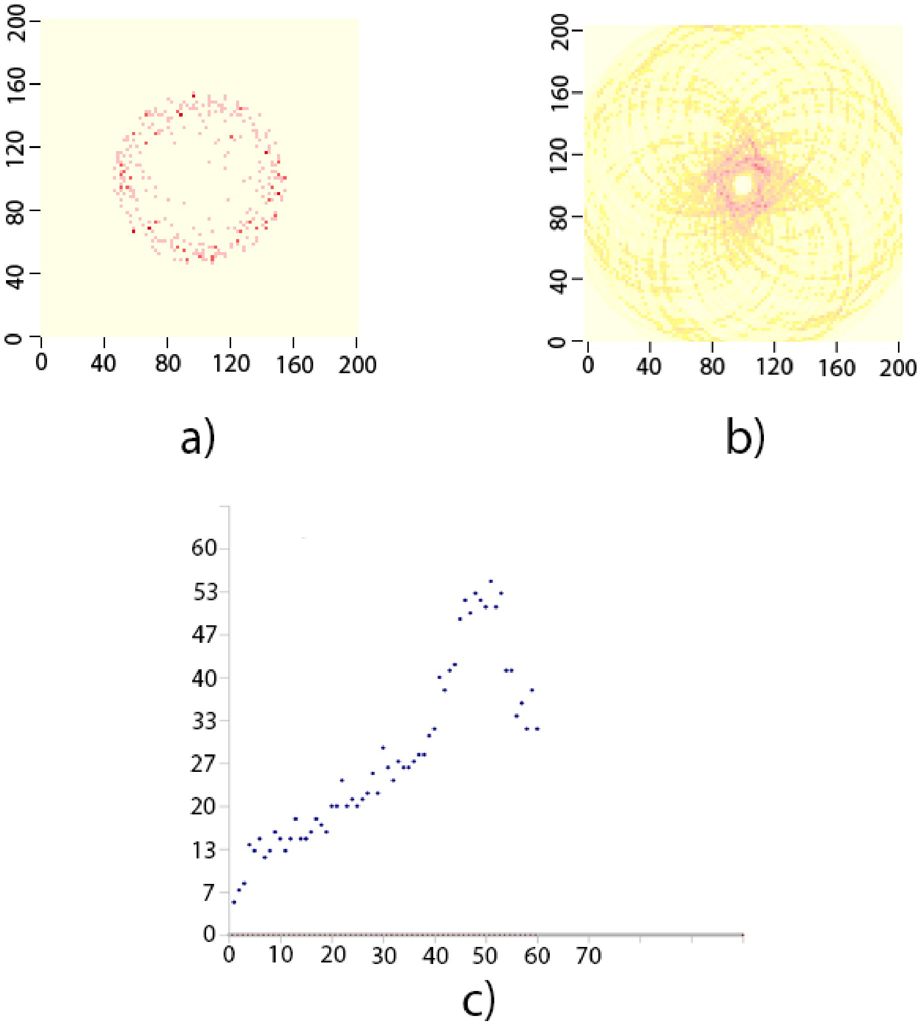

Figure 3.5: A Cherenkov cone is generated (panel a) by simulating the Cherenkov radiation for a Silicon based detector, with PMMA in front of it, having infinite resolution (refer to section 3.2). CHT is applied and the corresponding Hough space (panel b) points towards a likely value of the center and radius of the Cherenkov cone. The accumulator array can be plotted in a histogram to show the local maximum, which gives a value for the radius of the cone. Image generated by using GAMSIM II [4]

3.2 Testing the Validity of CHT with Simulations

Preliminary simulations were conducted to test whether the application of CHT was possible for the detection of Cherenkov cones. For this purpose, an open source Matlab code was chosen [36] as the base code. Due to the accurate results it was able to produce after comparison with other alternatives like the built in CHT functions in OpenCV and Matlab itself along with its ease of use. Certain fixes were implemented in the program to make it faster. These fixes included the addition of correct radial scan which the user provided, passing completely binary data sets or image arrays to the program instead of images among some other bug fixes. The first step was to simulate circles generated by Cherenkov cones incident on a detector with infinite spatial resolution (section 3.2.1). However, since the actual detector has a finite spatial resolution of 3 mm for one channel (see section 4.1.1), runs were made to simulate circles generated by Cherenkov radiation falling on a detector which has a limited spatial resolution as well (section 3.2.2).

The algorithm was then tested with different circle generating algorithms, where each run contained 1000 data sets each to increase statistics. The corresponding radii found applying CHT were then plotted in a histogram for each single run to see the deviation from the actual provided radius.

3.2.1 Circles with Infinite Resolution

The test of the validity of a CHT for the detection of Cherenkov cone was done in steps with each run employing a modification over the previous algorithm.

Run 1

For the beginning a simple algorithm was designed to generate random points, using uniform random number distribution, around the perimeter of a circle. They were plotted in a circular area of ±20% for each point around the perimeter of a circle whose radius, 192 pixels, was provided. For each data set 360 points were generated, one for each degree of the circle. CHT was then applied to detect the radius of the circle. Figure 3.6 shows the data generation flowchart to explain the basic algorithm used for this process.

A 1000 events were generated in such a way and CHT was applied afterwards on them. The applied CHT was programmed to give a single radius and center point values in pixels. A circle with those parameters was then drawn over the generated data providing a visual representation of the success of the method. A single data set along with its results are shown in Figure 3.7. The histogram of the detected radii for all 1000 events is shown in Figure 3.8. The calculated radius from Matlab's native axis was 192 pixels, while the mean of 1000 runs gave a result of 193.3 pixels by applying the CHT.

The disparity arises due to the limitation of the applied CHT, as it can only process radii as integers in pixel units along with the uncertainty in converting native, arbitrary Matlab axis to pixel units. In later versions of the program, the process of passing generated data sets to CHT algorithm was improved to not only increase precision but also decrease the overall processing time for the CHT to give results.

Run 2

Since CHT was intended for the detection of Cherenkov cone circles, amendments were made to the data generation algorithm. The radius of the cone from Cherenkov radiation decreases as the energy of the initial particle decreases. In order to simulate this behavior in run 2, 1000 more data sets were generated similar to run 1, however this time, whenever a random point was outside the given radius of the original circle (192 pixels), it was flipped 180^o in the small circular area. This way points were randomly scattered towards the inner area of the circle with a maximum radius of 192 pixels. One example is shown in figure 3.9 (a). CHT was applied over the generated data sets and the resulting radii were again plotted in histogram form, see figure 3.10, with the detected circle drawn over the data, figure 3.9 (b).

As it can be seen from figure 3.10, the mean of the histogram shifts significantly towards a lower value with a slight tail. This can be explained by the points being flipped if they were greater than the original radius of the circle.

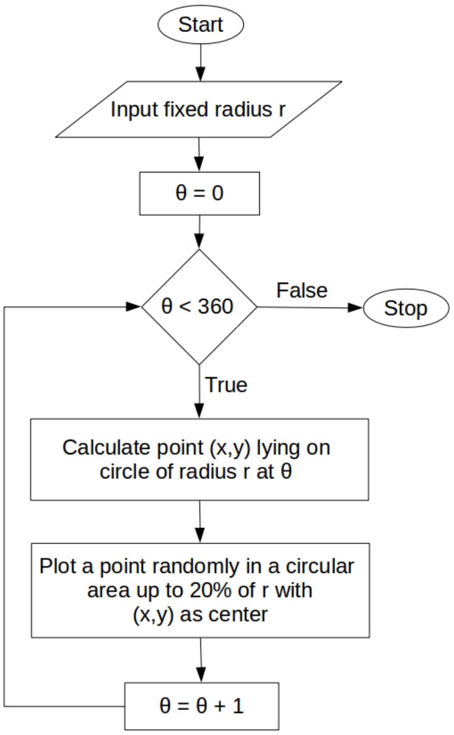

Figure 3.6: Flowchart mapping the data generation process for one data set.

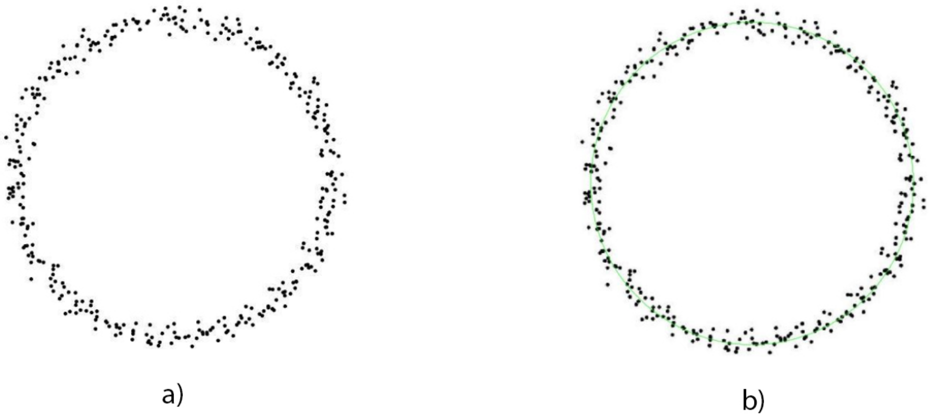

Figure 3.7: Panel a shows the circle generated by the algorithm, while panel b shows the results of the applied CHT (green circle).

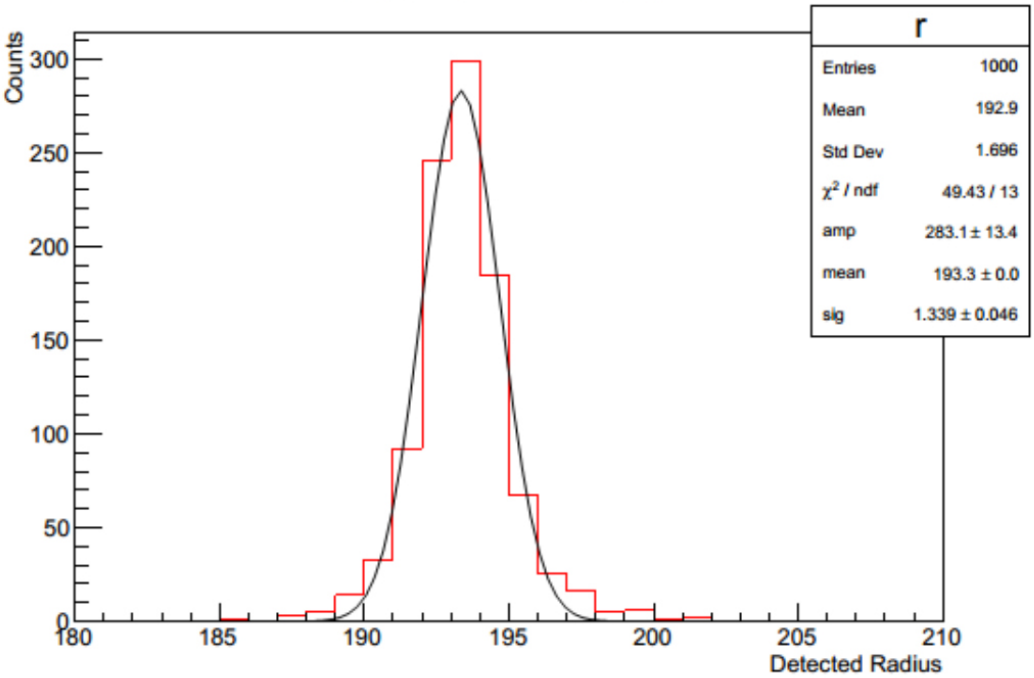

Figure 3.8: A histogram showing the detected Radii vs total counts for a total of 1000 data sets. A simple Gaussian fit is applied over the histogram to get the mean value.

As a result, the applied CHT has a tendency to detect circles which are smaller than the actual one. The shift however, still lies in an appropriate error margin as the SiPM chosen (see section 4.1.1) does not have infinite resolution. The error when converted to distance in mm, comes out to be 0.53 mm approximately by rounding off, which is far less than the spatial resolution of the SiPM (3 mm) chosen for the experiment. The actual circle after conversion was of 50.8 mm radius. Pixels can be converted to mm by using the equation:

$$distance(mm) = \frac{pixels\ 25.4}{dpi} \tag{3.2}$$

Where pixels is the pixels you want to convert, dpi represents the dots per inch of the image, which for this case is 96 and 25.4 is a conversion factor that arises when converting inches to mm.

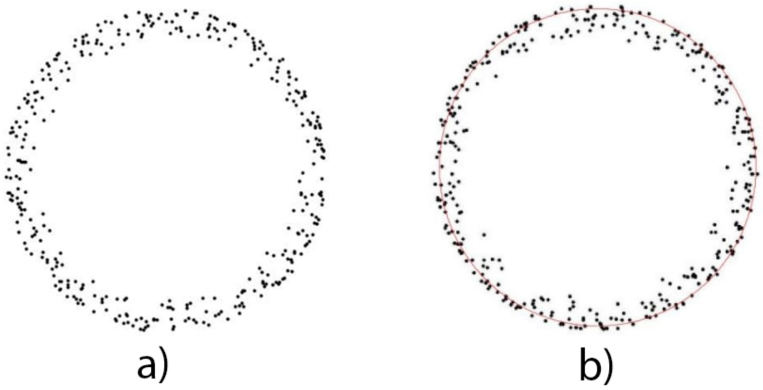

Figure 3.9: Panel a shows the raw data set passed to the CHT whereas panel b shows the detected circle drawn in red.

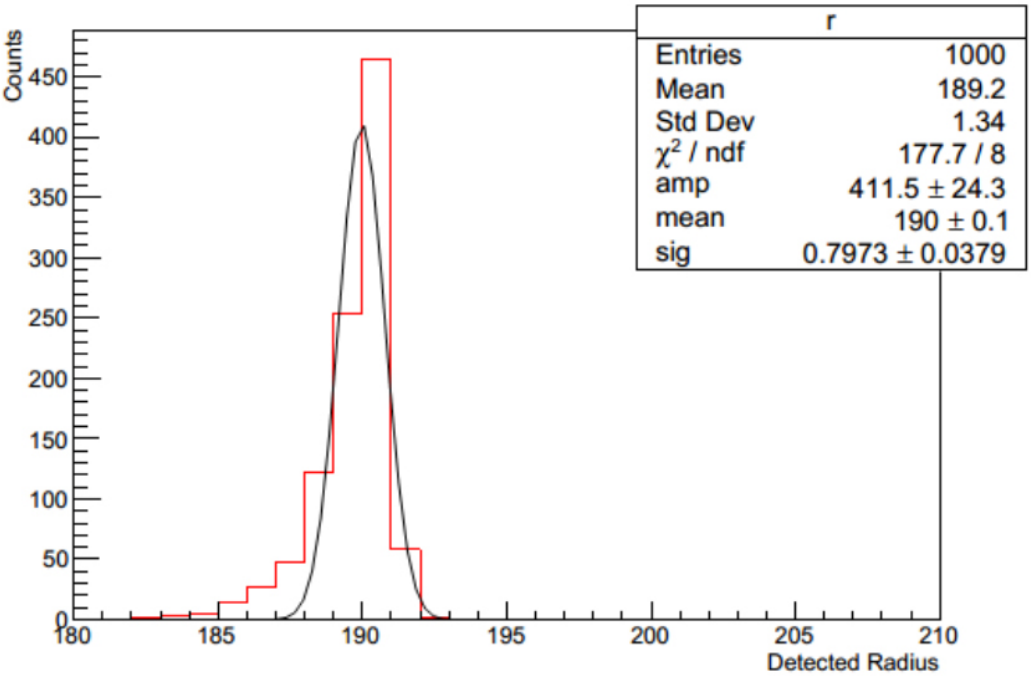

Figure 3.10: A histogram showing the detected Radii vs total counts for a total of 1000 data sets. A simple Gaussian fit is applied over the histogram as only the mean value which provides the radius that has the highest probability of being detected by the applied CHT is interesting.

3.2.2 Circles with Finite Resolution

Up till now, it was assumed that the detector had infinite resolution and only perfect circles with no pixelation would be detected. However, as explained in section 4.1.1, the detector does have a limited resolution and as a consequence pixelation is expected. To incorporate this into simulation and test the validity of the application of CHT, more runs of 1000 data sets were performed, which are summarized into a single run below.

Run 3

Algorithm: For generating data from a pseudo detector with limited resolution, the algorithm from Run 2 was modified by dividing the whole image into grid sections. Each randomly drawn point was shifted to the center of each grid box. This limited the resolution of the "detector" and gave pixelated images. Another thing to consider was the reduced photon detection efficiency of the detector itself. To take this into consideration, alterations were made so that random number of points were taken for each of the 1000 runs. The number of points ranged from 3 to 360 and were decided by a uniform random number distribution individually for each data set. The minimum was set to 3 points as the CHT needed at least a minimum of 3 points to define a circle. Figure 3.11 shows the algorithm in flowchart form, whereas figure 3.12 illustrates the process alongside the resulting image.

The algorithm for these runs was improved significantly. Instead of generating images and passing them to CHT, binary image arrays were produced and used for applying the transform. This dramatically reduced the processing time by 1/3. As a consequence, the images generated are shown in figures 3.12 and 3.13 with black background (0) with white pixels (1).

Results: For 1000 data sets, with a grid size of 20 pixels, the histogram depicting the detected radii is shown in Figure 3.14. The histogram shows a mean of 190.5 pixels which compared to the original 200 pixel radius given. This however, was an anticipated result as the error was bound to increase with pixelation. There was also an offset of 2 pixels for the center of the circle found by CHT for all data runs. This also can be attributed to the pixelation of the image as well as the reduced number of points. Both of these errors increased for a larger grid size, but as it was found out they followed the same pattern as the one shown in Figure 3.14 and 3.13 and consequently could easily be reduced by adding a certain offset in the detected radii for each grid size in the CHT.

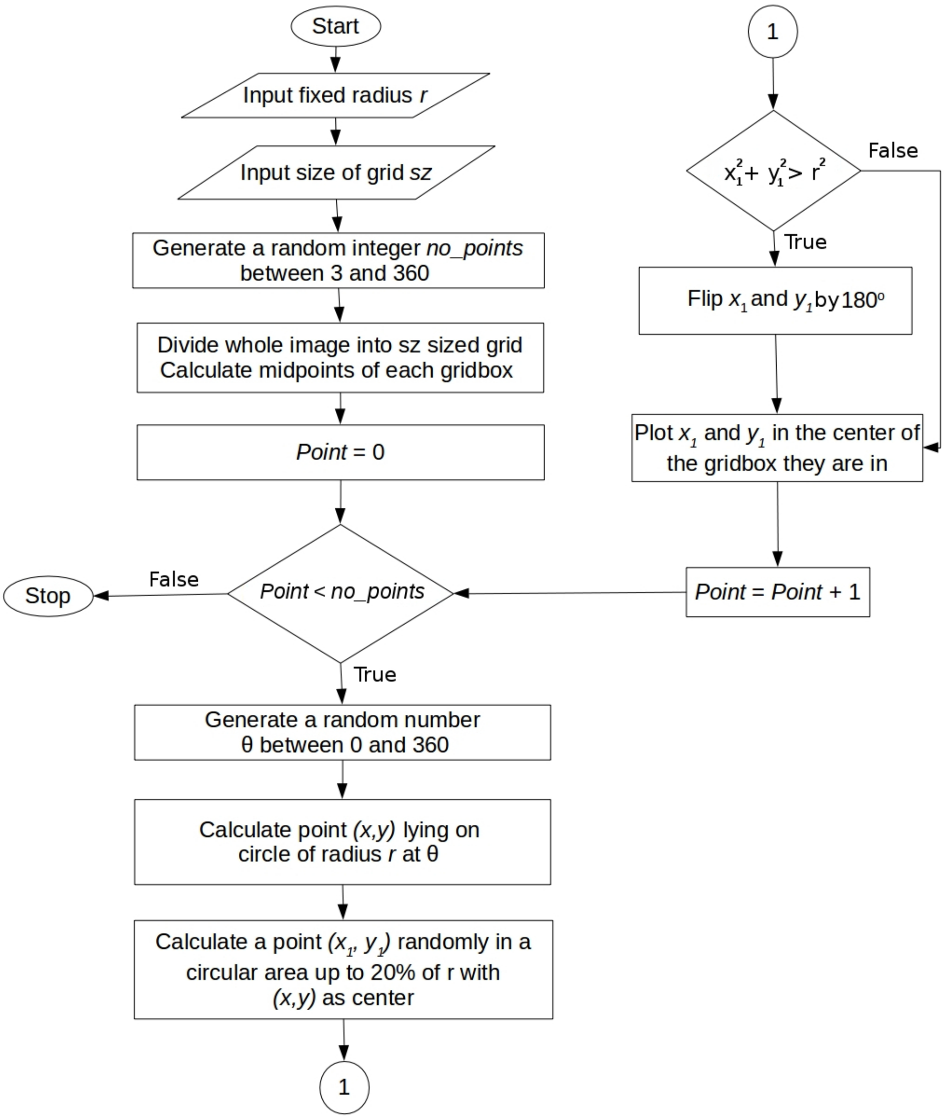

Figure 3.11: Flowchart detailing the logic followed for Run 1 for creating circles with finite resolution and limited photon detection efficiency

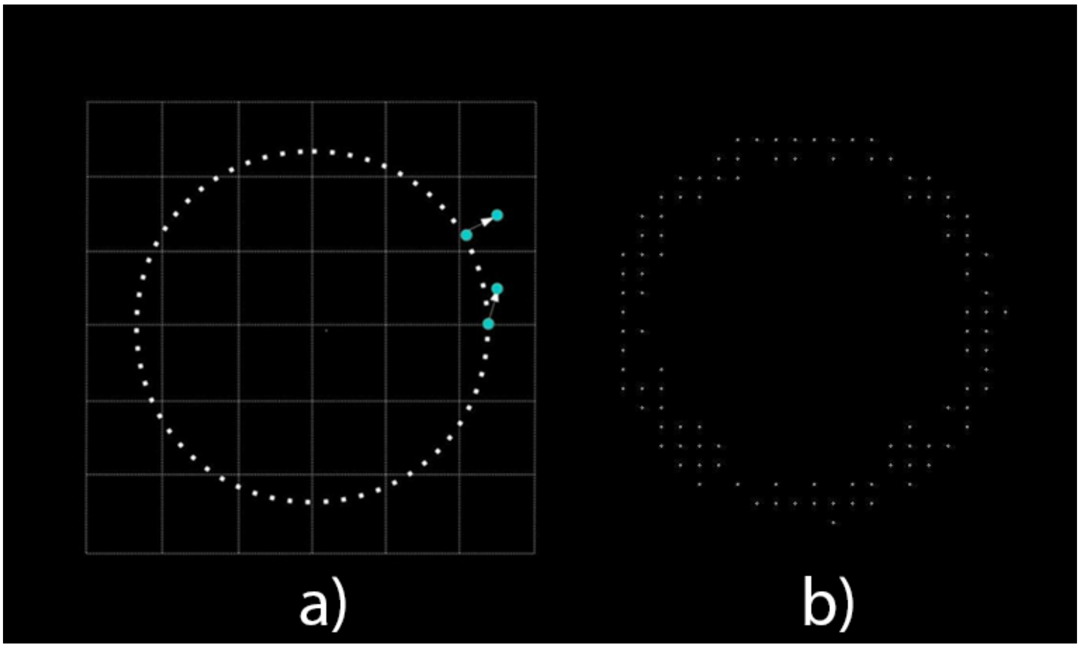

Figure 3.12: Panel a) depicts the process of moving points of a circle to the center of the grid (not to scale), whereas panel b) shows the output image generated with a much smaller grid size than the one shown in panel a.

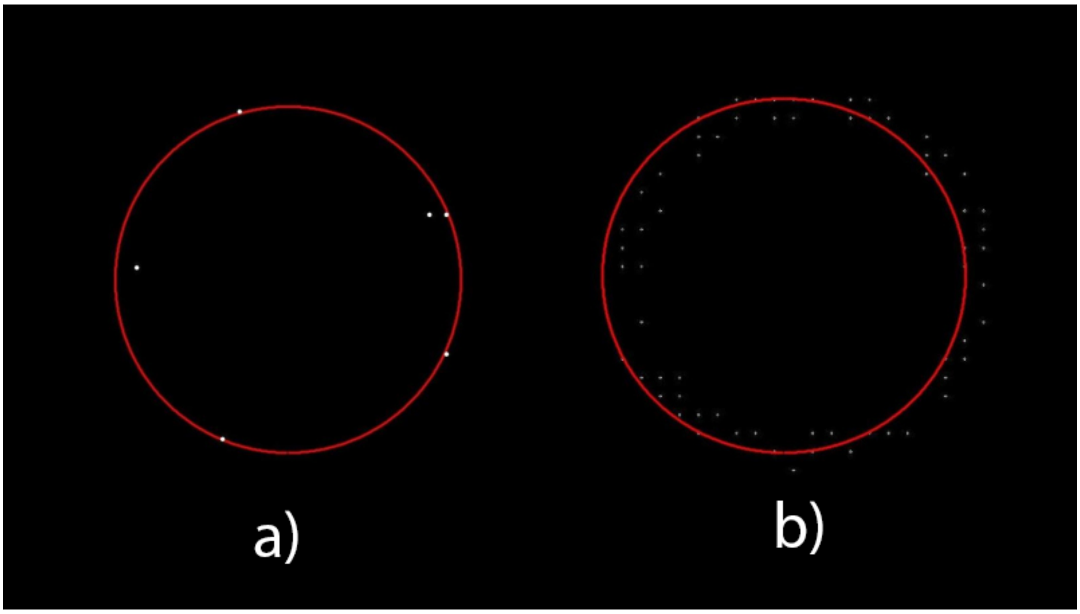

Figure 3.13: Figure depicting the results from CHT shown via the red circle. There is a small offset, which appears due to pixelation, between the original center and the one found by CHT

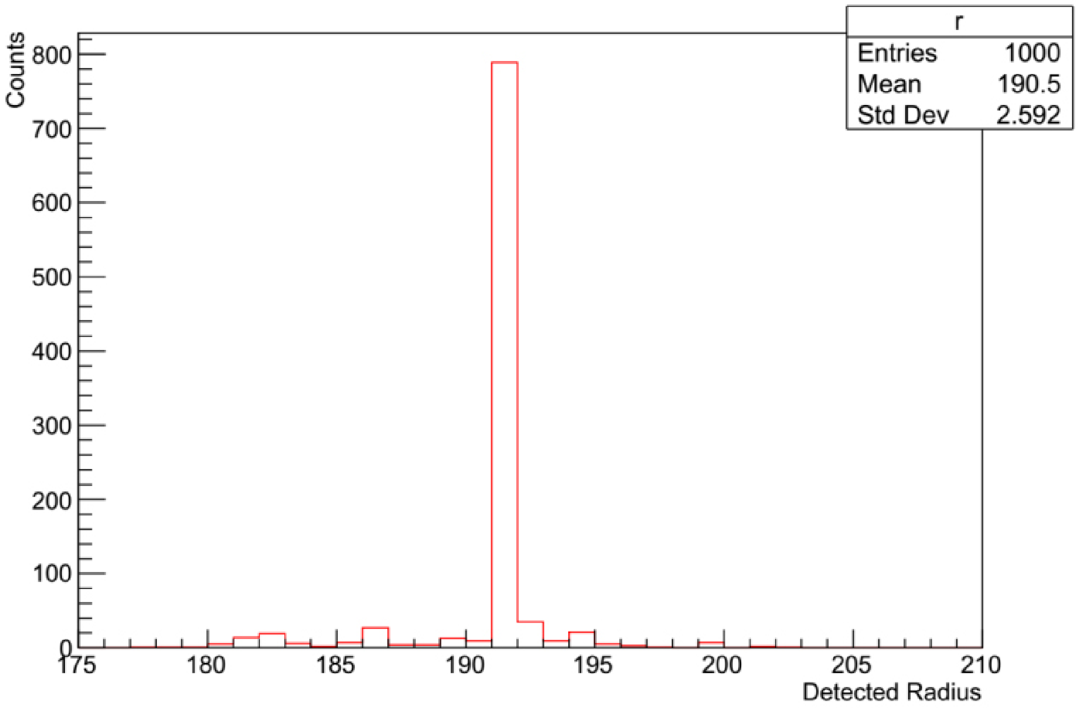

Figure 3.14: Histogram depicting the results of 1000 data sets. The CHT tends to detect smaller, shifted circles due to pixelation.

3.2.3 Conclusion

Some preliminary studies were conducted to test the validity of detecting a Cherenkov cone by using a Circular Hough Transform (CHT) by employing different algorithms. Each algorithm was programmed to generate 1000 data sets, which were then passed to the CHT applying program. The results were then plotted in a histogram format to obtain the mean value for each run of 1000 data sets. With each progressive run, different parameters i.e. the degradation of cone size due to energy loss, limited position resolution of the detector, and generating binary images or arrays were introduced in attempts to test the transformation technique as well as to reduce the processing time. Mean radii detected for each run along with their errors are given in Table 3.1.

It was concluded from the summary in Table 3.1, CHT was a valid technique for the purpose of circle detection generated by Cherenkov photons, provided the data was passed in binary images or arrays to the program. Attempts were also made to test the validity of the algorithm for the detection of ellipses, which are generated by electrons entering the material at an angle. However, the results were not ideal and the processing time of the program increased by a factor of 10 or more, depending on the data provided. Therefore, it is suggested to use either a different technique altogether for general ellipse detection or to employ certain special tricks to increase overall detection efficiency while simultaneously being able to reduce the size of unknown variables. Doing this will allow to reduce the accumulator array for an ellipse and consequently be able to provide with an amiable overall processing time.

Run	**Given Radius** (pixels)	**Detected Radius** (pixels)	Δr (%)	**Offset** (mm)
1	192.5	193.3	0.4	0.21
2	192.5	190	1.3	0.6
3	200	190.5	4.75	2.5

Table 3.1: Table summarizing the results of all runs of simulations made. Each run consisted of 1000 data sets. Here, Offset refers to the deviation of the detected radius with the provided one in mm. Note: Run 3's data consisted of an average of 3 simulation runs with 1000 data sets with an algorithm that varied slightly from its predecessor.

3.3 Multiple Scattering Simulation

To understand the deviation of the electron from its original trajectory due to multiple scattering, simulations were made in Matlab. A 3mm thick material with an average atomic number of 6 and average atomic mass of 12 was simulated. Since most plastics are long carbon chains, this provided a good approximation to study the effects of total multiple scattering on the original path of the electron.

For this thickness, first the total cross section for multiple scattering, both Coulumbic and Rutherford, was calculated for the material to give a mean free path of the electron. The mean free path defines the number of encounters per track length. After the calculation of mean free path, the program was made to loop over the total number of electron interactions. In each iteration, a Monte Carlo technique was used to calculate the scattering angles using the probability functions of equation 2.9 and 2.10 as the random numbers generated were equally distributed between $[0\,,1]$ [37]. The probability functions allowed the calculation of the scattering angles for the material which were accumulated in an array and are shown in histogram form in figure 3.16.

Results The results were as expected, as a Gaussian distribution with a small tail was observed(see section 2.2). This was tested for different energies and compounds, the results however remained the same. This meant that the initial assumption that the electron would slightly deviate from its original path at high energies and mostly encounter small angle scattering was correct. The purpose of this simulation was to enhance the understanding of the positioning of the Cherenkov photons on the actual SiPM detector and observe if large deviations from the original path were expected.

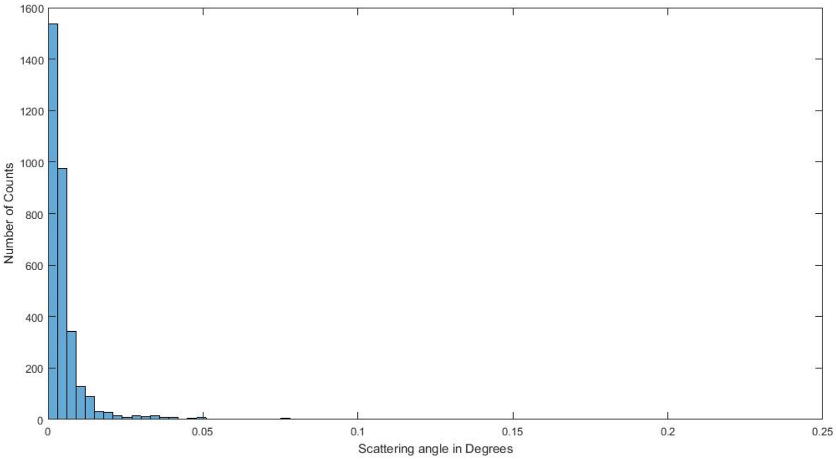

Figure 3.15: Histogram depicting the scattering angles of a 1 MeV electron traversing through a 3 mm material of Z = 6, A = 12.

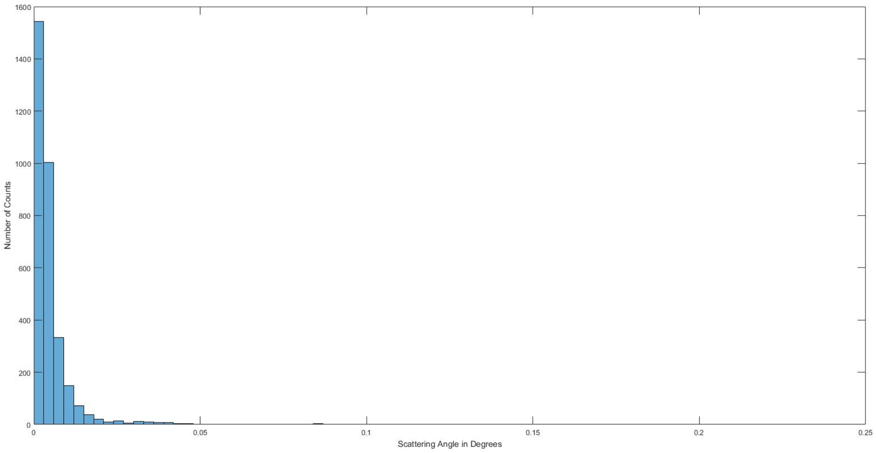

Figure 3.16: Histogram depicting the scattering angles of a 2 MeV electron traversing through a 3 mm material of Z = 6, A = 12.

Chapter 4

Experimental Setup

In this chapter the experimental setup along with a brief introduction to various key components such as the SiPM array, electronic readout system and their relevance to the experiment will be explained.

4.1 Components

The measurements presented in this thesis were taken in a dark box with a SiPM array connected to an electronic readout system. The purpose of the dark box was to provide the darkest environment possible for the SiPM, so to lessen the dark count rate as much as possible. The two main electronic readout systems used for measurements were an ASIC (Application Specific Integrated Circuit) chip with its evaluation board and an oscilloscope that was connected to the SiPM array using a connector board.

4.1.1 SiPM Array

The SiPM array selected for the experiment was a 4x4 array (S13361-3075AS) from Hamamatsu. This specific SiPM array had the dimensions of 13x13 mm^2 with each channel being 3x3 mm^2, as shown in figure 4.1 and 4.2. The SiPM array was selected due to its lower dark count rate, decreased cross talk between channels and increased sensitivity in ultraviolet range (see section 2.2.2) compared to the previous generation of MPPCs from Hamamatsu [38]. Some key characteristics of the SiPM array are listed in table 4.1 as well as Appendix A.

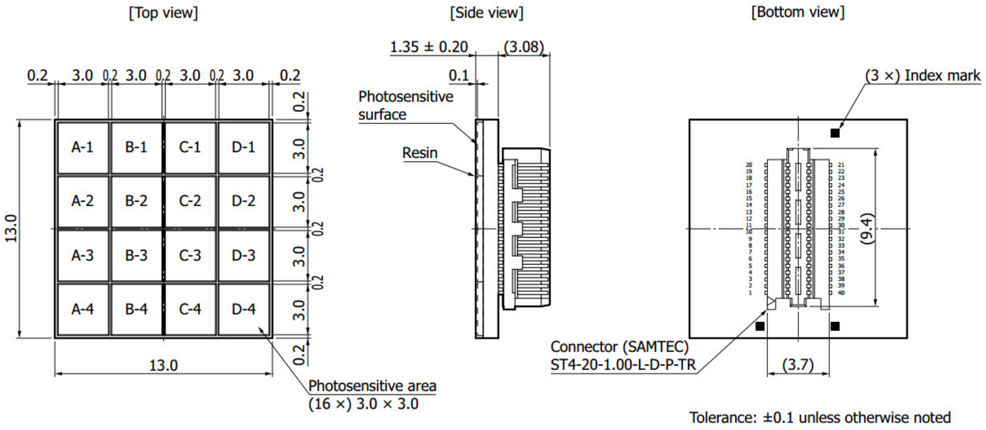

Figure 4.1: A schematic drawing of the SiPM array. Here A-1 to D-4 represent the 16 channels of the SiPM array. Each measurement is in mm [39].

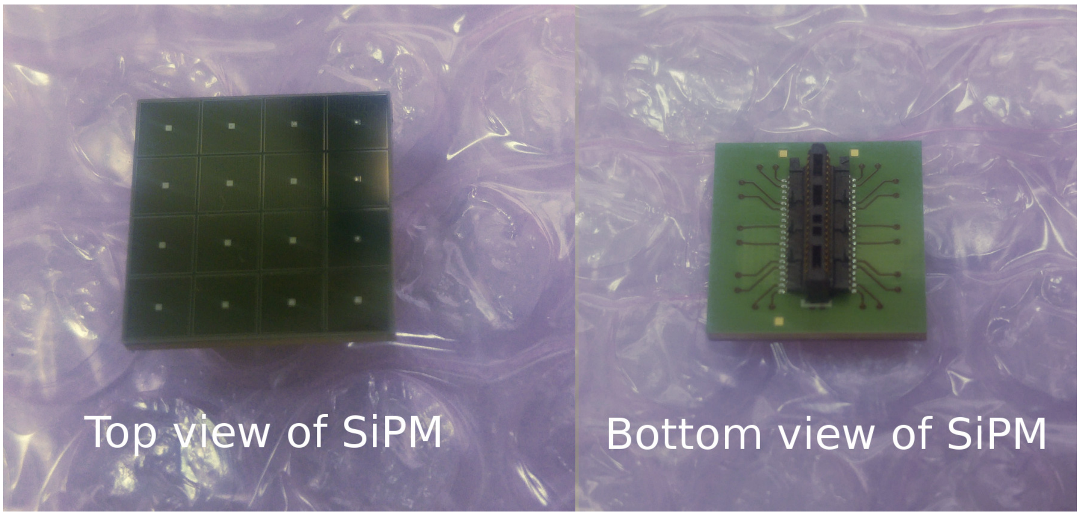

Figure 4.2: S13361-3075 MPPC array from Hamamatsu used in the experiment. The array has 16 channels (one small black square in the top view) and can be mounted on top of a special connector to provide it with high voltage and to read out data.

Parameter	**Value**	**Unit**
Spectral Response Range	320 to 900	nm
Peak Sensitivity Wavelength	450	nm
Photon Detection Efficiency	40	%
Dark Count per Channel	0.40 - 0.66	Mcps
Average Breakdown Voltage	52.5	V

Table 4.1: Table summarizing some of the key characteristics of the SiPM array as provided by Hamamatsu [38]. All data is taken at 25^o C with 3 V over voltage.

The SiPM array was mounted on top of either the ASIC evaluation board or a signal read out board designed by the electronics lab in University of Siegen. Both of these setups were capable of providing the MPPC array with the high voltage it required to function as well as to transfer its analog data to the read out electronics.

4.1.2 STiC3 ASIC Chip

One of the main electronic readout systems for the experiment was chosen to be the STiC3 ASIC Chip designed by the Kirchoff Institute for Physics, University of Heidelberg. The ASIC was designed for the detection of scintillation light by using scintillating crystals coupled with SiPMs from a ^{22}Na source for the development of an endoscopic PET detector. The chip itself is bonded on a small daughter board (a cavity MCM module) of 25 x 25 mm [40]. The module along with its evaluation board are shown in figure 4.4. The evaluation board consists of a FPGA board and a power regulation circuit for the STiC3 chip. The STiC3 chip can read up to 64 channels or four 16 channel SiPM arrays simultaneously.

Basic Working Procedure:

Analog data from the SiPM array is converted to digital signals via Time to Digital Converters (TDCs) mounted on the FPGA present on the evaluation board. A signal is recorded with the help of a trigger logic, as shown in figure 4.3. The STiC3 uses two discriminators with individual thresholds, the time discriminator provides a precise time trigger signal whereas the energy discriminator gives the Time-over-Threshold (ToT). ToT of a pulse from the SiPM is calculated by evaluating the time difference between the rising edge of T-Threshold and the falling edge of E-Threshold [41]. The signal is then combined in a single TDC channel using a XOR combination and the timing and charge information is stored as Time and Energy stamps respectively by the STiC3 chip. The timing resolution of the STiC3 chip is calculated to be 200 ps [42], making it a suitable candidate for not only detecting Cherenkov photons but also being able to distinguish Cherenkov light from scintillation light.

The output of the STiC3 is sent to a computer via USB 2.0, where a GUI setup can be used to change various parameters such as the aforementioned thresholds for all channels separately. A secondary software is available for viewing data in real time and data acquisition by saving the data in the form of ROOT files [40].

Since the STiC3 chip was designed for the detection of scintillation light, time over threshold measurements for single photons with the ASIC is impossible [41]. Therefore, if STiC3 is used in normal operational mode, some percentage of the signal from Cherenkov photons will be lost. However, single photon resolution can be achieved by using a special mode of the STiC3, in which only the T-Threshold is active and the E-Threshold is disabled. The mode is referred to as the "receive all" mode. In this mode all signals which are higher than the T trigger are recorded by the STiC3 chip. The STiC3 starts to record data whenever a waveform is higher than the set T-Threshold value. Since there is no second trigger, a signal is completed and stored whenever a second signal arrives which is higher than the set trigger value.

Originally the "receive all" mode was designed for conducting dark count scans to better characterize the STiC chip threshold levels as well as the SiPM itself but in principle it can also be used for the detection of single photon events. However, single photon resolution with the STiC3 chip is not preferred due to dark count rate. As there is no E-Trigger, the chip will trigger on dark count, which might present a problem in offline data analysis. It is therefore best to use the STiC3 in normal mode with a T-Trigger set at 2 pe level.

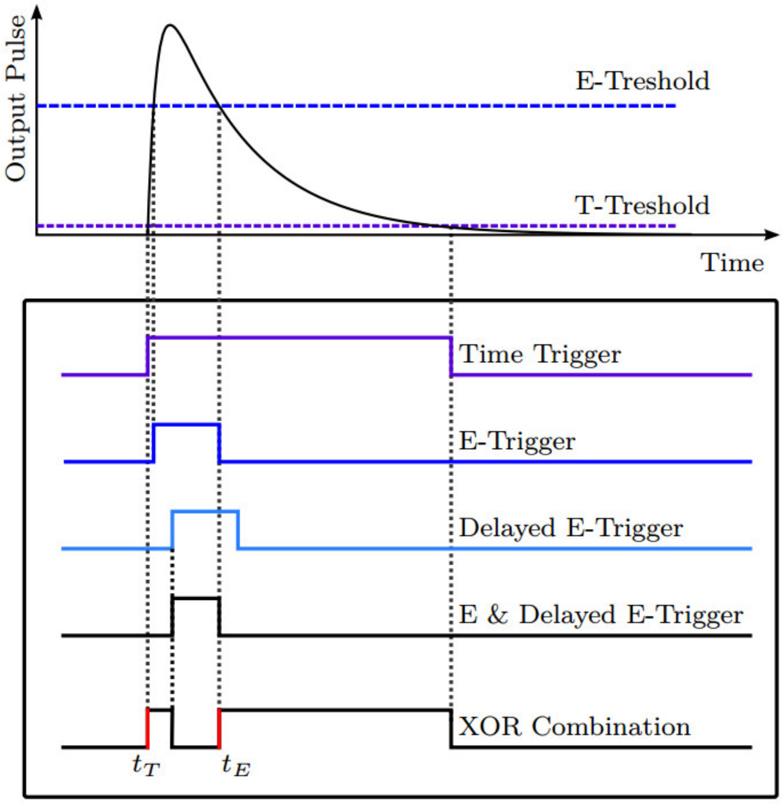

Figure 4.3: Signal waveforms during the trigger merging by STiC3 MCM [41]

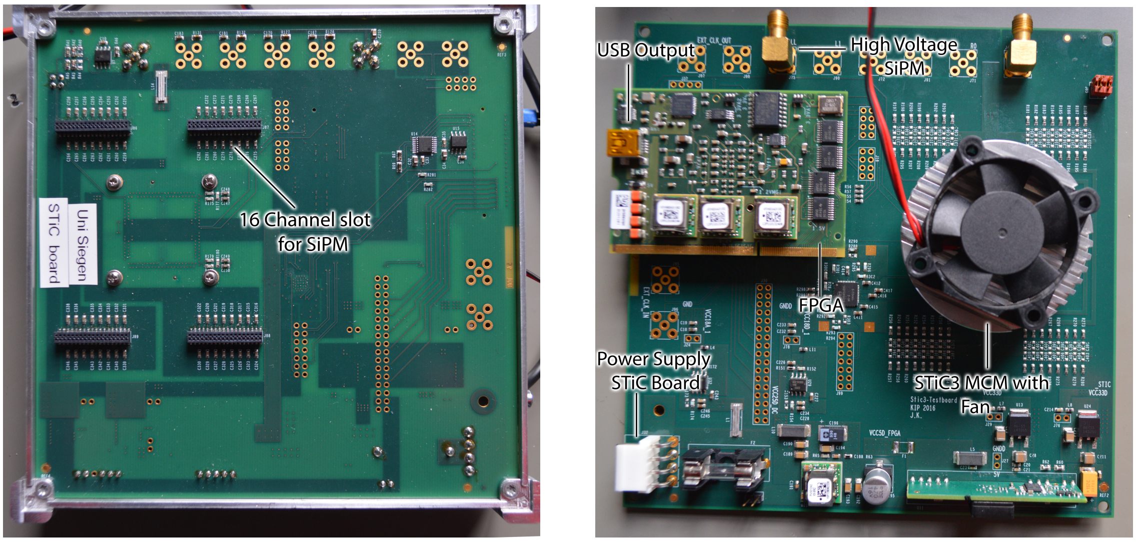

(a) Top of STiC3 evaluation board (b) Bottom of STiC3 evaluation board

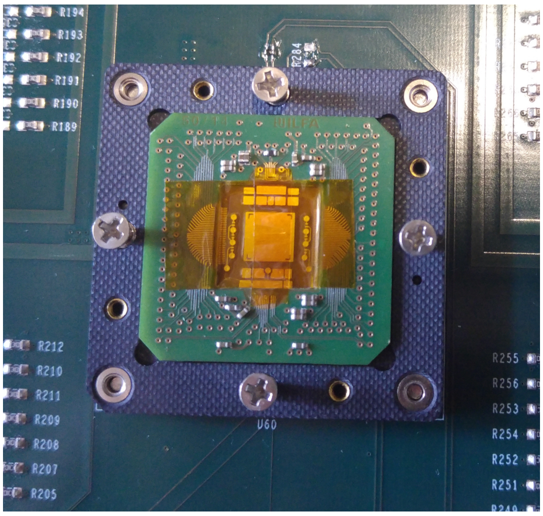

(c) STiC3 MCM module

Figure 4.4: STiC3 MCM and its evaluation board

4.2 Measuring Setup

As mentioned earlier, measurements were taken from two apparatuses, namely the oscilloscope and the STiC3 chip with its evaluation board. Both of these apparatuses are shown below to illustrate the measurement setup.

4.2.1 Oscilloscope Setup

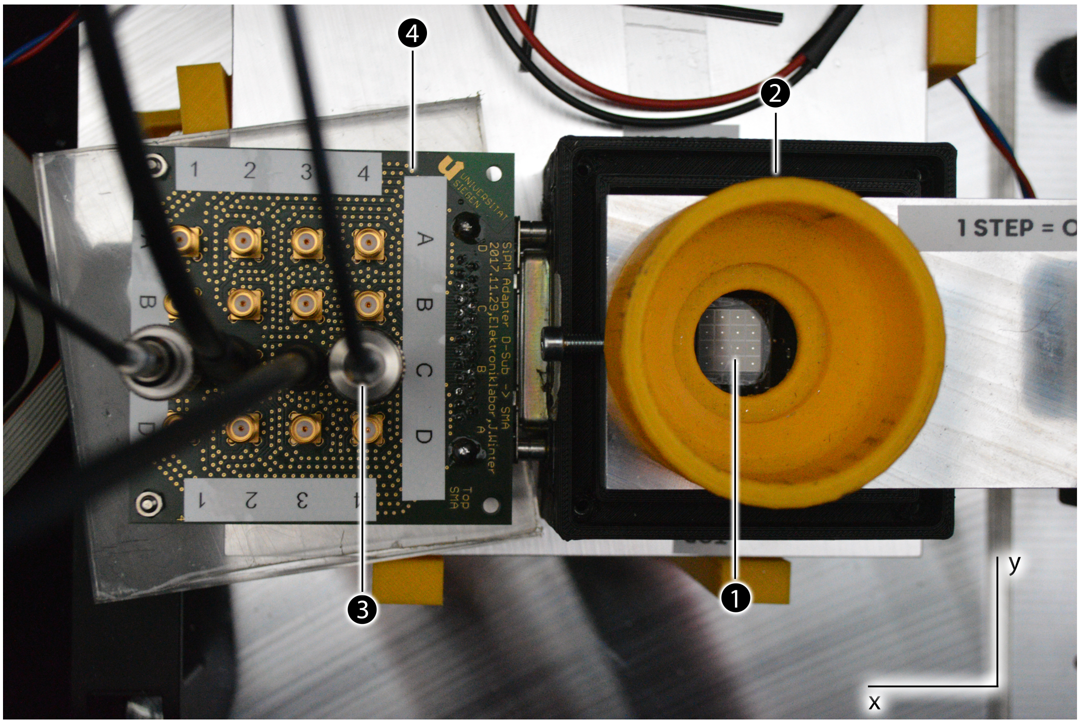

Figure 4.5: 1. SiPM array with 3mm thick PMMA on top. 2. Radioactive ^{90}Sr source holder connected to a step motor capable of moving in (x, y, z) directions with the coordinate frame shown in the bottom right corner. Z axis is pointing out of the paper. 3. Wires leading to the 4 GHz bandwidth, oscilloscope with 25 GS/s sampling rate. 4. D-SUB connector board with a SMA port for the output of each channel, marked by the stickers (see figure 4.1). The board was designed so each SMA connector has equal wire length from the D-SUB port.

4.2.2 STiC3 Setup

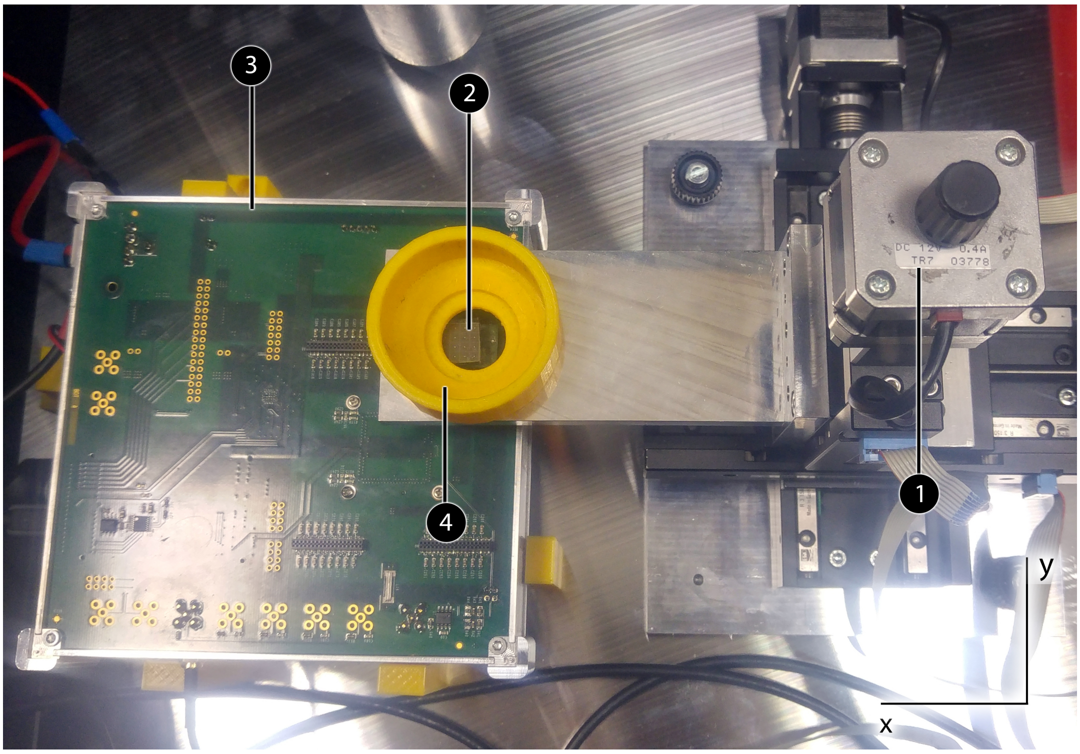

Figure 4.6: 1. Step motor capable of moving in (x, y, z) directions with the coordinate frame shown in the bottom right corner. Z axis is pointing out of the paper. 2. SiPM array mounted on top of the STiC3 evaluation board with a 3mm thick PMMA sample on top. 3. STiC3 evaluation board whose output leads to the computer. 4. Radioactive ^{90}Sr source holder connected to the step motor.

Chapter 5

Data Acquisition and Analysis

In this chapter the process of data acquisition and its analysis for the detection of Cherenkov light will be discussed. As explained earlier, the experimental measurements were done by two different readout electronics, the oscilloscope and the STiC3 ASIC. Before taking actual measurements with both setups, they were also tested to see if the detection of actual Cherenkov light was possible with the setup or not. These results will be discussed before the actual measurements for each setup.

5.1 STiC3 Measurements

Initial attempts to detect Cherenkov light using the SiPM array were made by using the STiC3 ASIC and its evaluation board from University of Heidelberg. As explained in section 4.1.2, the STiC3 setup was designed for the detection of scintillation light from a ^{22}Na source. The pre-made analysis code focused towards the detection of coincidences from 511 keV gamma photon-electron events and calculating the coincidence timing resolution between two coincident channels of two SiPMs [40]. Consequently, online data analysis with the available STiC3 software was not possible. Therefore a ROOT based analysis program was designed within the group. The program was capable of searching for coincidences from 16 channels of the SiPM array within a certain coincidence time window, storing the relevant time over threshold information for energy spectra analysis and drawing the coincidences of all 16 channels in the form of 2D color intensity plots and 3D lego histograms.

5.1.1 Dark Count Rate (DCR) Scans

It was decided to use the STiC3 setup initially for the measurement of 2 to 3 photon events in normal operational mode and then attempt to achieve single photon resolution in the receive all mode (see section 4.1.2). To get an estimate value for the first trigger (T-Threshold as shown in figure 4.3) such that at least 2 to 3 photon events were being triggered on, DCR scans were done for all 16 channels of the SiPM array. Only after an idea of where to set the T-Threshold trigger, could the second trigger (E-Threshold) be set to record proper signals in the normal mode.

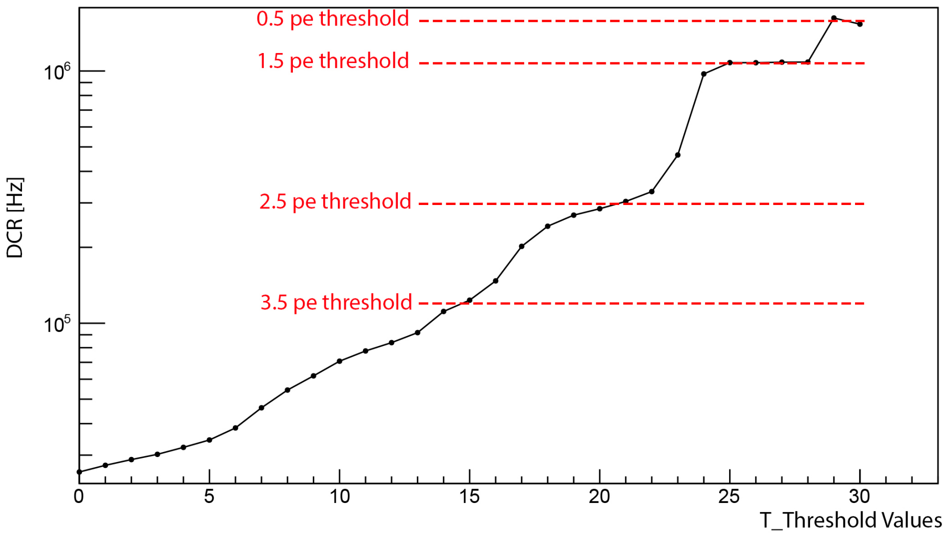

Figure 5.1: The dark count rate is plotted against the corresponding T-Threshold value and displayed in log scale. The 0.5, 1.5, 2.5 and 3.5 photoelectron thresholds are marked by horizontal lines.

To conduct DCR scans, the setup was placed inside a dark box with the SiPM array covered by an additional black plastic cap to ensure no light could get through and the STiC3 chip was put in the receive all mode. As a reminder, the receive all mode is a mode in which the E-Threshold trigger is completely ignored and T-Threshold values are ramped one by one. Usually the T-Threshold values go from arbitrary software integer values of 0 to 32 but the range can vary for different channels. The data is then stored in the form of a ROOT file for a single T-Threshold value. These files can then be analyzed offline to determine the DCR. Another important thing to note is that the T-Threshold values are reversed in the STiC3 software, meaning a value of 0 corresponds to a physically higher T-Threshold trigger and vice versa a value of 32 corresponds to a physically lower T-Threshold trigger value. Therefore, by ramping the values of T-Threshold in succession sees the DCR increase until the STiC3 setup starts to trigger on electronic noise.

The collected data for DCR scans was analyzed using a pre-made analysis script which was able to calculate the DCR for each T-Threshold value. Events which had an event rate of less than 70 kHz, had their DCR calculated by simply counting the total entries and dividing by the entry number with the acquisition time. Whereas, events which had a rate higher than 70 kHz had their DCR calculated by fitting an exponential function to the timing difference plot [40]. The dark count rates were then plotted in a single graph against their corresponding T-Threshold values, as shown in figure 5.1 (for a single channel).

As seen in figure 5.1, the resulting graph of T-Threshold values vs. DCR gave a step function where each higher step corresponded to a lower photoelectron threshold till electronic noise level (0 pe) was hit [43]. From this graph, the T-Threshold value for three pe level was approximated to be 17 for this specific channel. Similarly, the corresponding three pe T-Threshold values were found for all 16 channels.

5.1.2 Cherenkov Light Detection using STiC3

After calculating the appropriate T-Threshold values for all 16 channels using DCR scans, some initial calibration attempts were made on the STiC3 chip to set it up for the detection of events which were higher than 2 to 3 pe level. For this purpose, a 3 mm thick PMMA sample was optically coupled to the SiPM array, which was then connected to the STiC3 board (as shown in figure 4.7). A collimated ^{90}Sr was then placed just above the PMMA and measurements were taken after calculating the theoretical maximum radius of the Cherenkov ring.

Theoretical Estimation

The maximum radius of the Cherenkov cone was calculated by approximating the source can emit electrons at a maximum energy of 1.8 MeV. The Cherenkov angle (equation 2.16) and consequently the radius of the Cherenkov ring could then be calculated. For PMMA, the maximum radius then comes out to be 2.83 mm with a Cherenkov angle of 43.34^o. Since the size of one channel of the SiPM array is 3 mm, a collimated source pointed in the center of the array would generate a Cherenkov ring that would cover 4 neighboring channels simultaneously for a 3 mm PMMA.

Measurement with the Source Centered

For the first case, the collimated ^{90}Sr source was made to point towards the center of the SiPM array. It was expected that the outer channels of the array should be quiet while the center four channels see the most coincidences, as per the calculation done above. Data was recorded for 20 minutes and then analyzed offline. A coincidence event was recorded whenever there was a signal on two channels within 1.6 ns of each other. The number of coincidences detected on each channel were drawn in a 3D lego plot and a color intensity 2D histogram as shown in figure 5.2.

As seen in the figures, two central channels (10 and 11) saw the majority of the coincidences. As it was later found out from further readings, this discrepancy occurred due to the imperfect calibration of the STiC3 chip. However, for the beginning this was a relatively nice result as fewer coincidences on other channels of the SiPM array pointed towards low scintillation light yield.

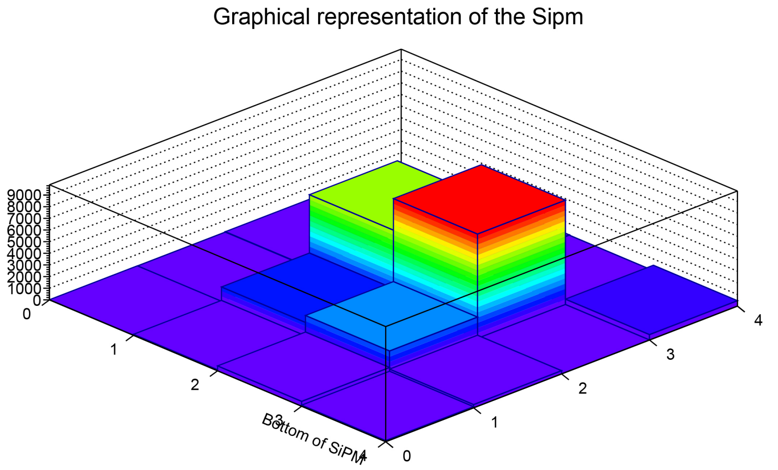

(a) 3D plot for coincidences seen by the SiPM array

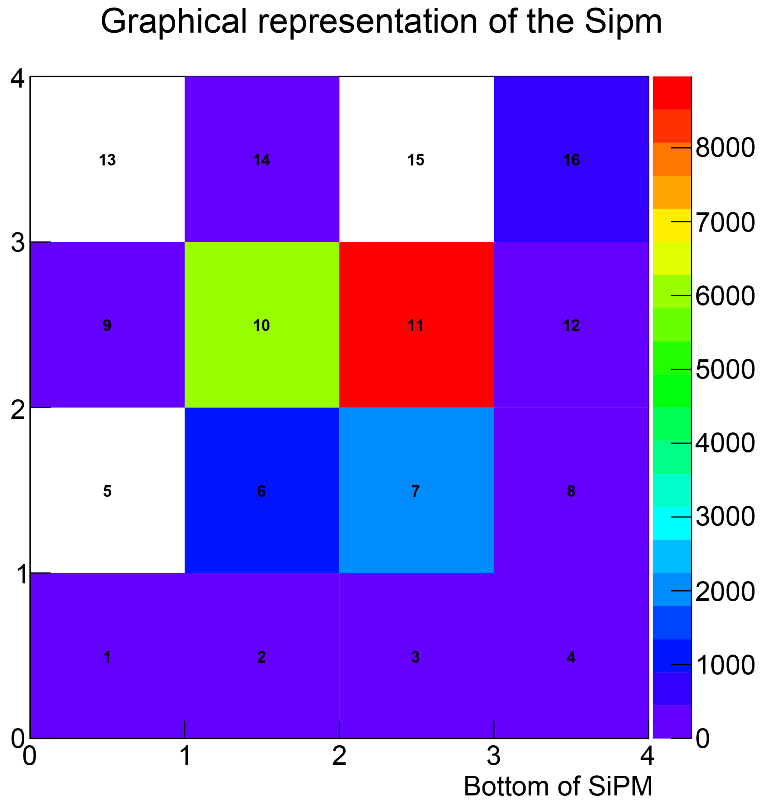

(b) 2D plot for coincidences seen by the SiPM array

Figure 5.2: Measurements recorded by keeping the source pointed to the center of the SiPM array. The channels of the SiPM array are marked from 1 to 16.

Measurements with the Source Moved

Further measurements were conducted by moving the source first towards the bottom left part (-3 mm in x and -6 mm in y direction from center of array, see figure 4.6) of the SiPM array and then towards the bottom right part (3 mm in x and -6 mm in y direction from center of array) using the step motor. The source was placed such that only the corner channels of the SiPM array would see any light from Cherenkov radiation. The same calibration of thresholds and coincidence time window was used for all measurements as before. The recorded results are shown in figure 5.3 and 5.4 respectively.

As it can be seen from the results, the movement of the source could be tracked on the SiPM surface with the movement of the Cherenkov circle.

Finally, the source was moved towards the top part of the SiPM array (0 mm in x and 3 mm in y direction from center of array) and again 20 minutes of data was taken. The results are shown in figure 5.5. As seen, the results were far from optimal as channels 14 and 15 showed little to no coincidences, whereas channel 16 showed more. By looking at the graphical representation and having no prior information about the experimental setup, it was difficult to make an estimation about the position of the source.

Considering the problems stated above, these results confirmed the suspicion that the calibration of the STiC3 chip was not proper as some channels saw more coincidence counts than others and were more sensitive due to their T and E trigger threshold being too low. However, due to technical difficulties which made the STiC3 chip unusable, further calibration attempts of the setup could not be made in the scope of this Master's thesis.

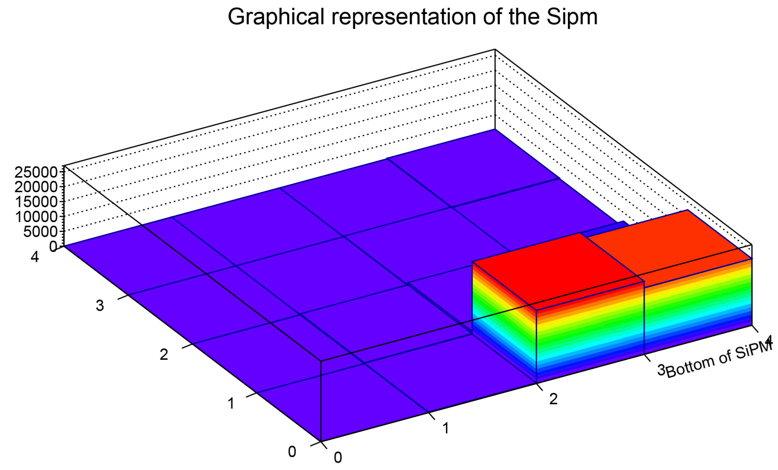

(a) 3D plot for coincidences seen by the SiPM array

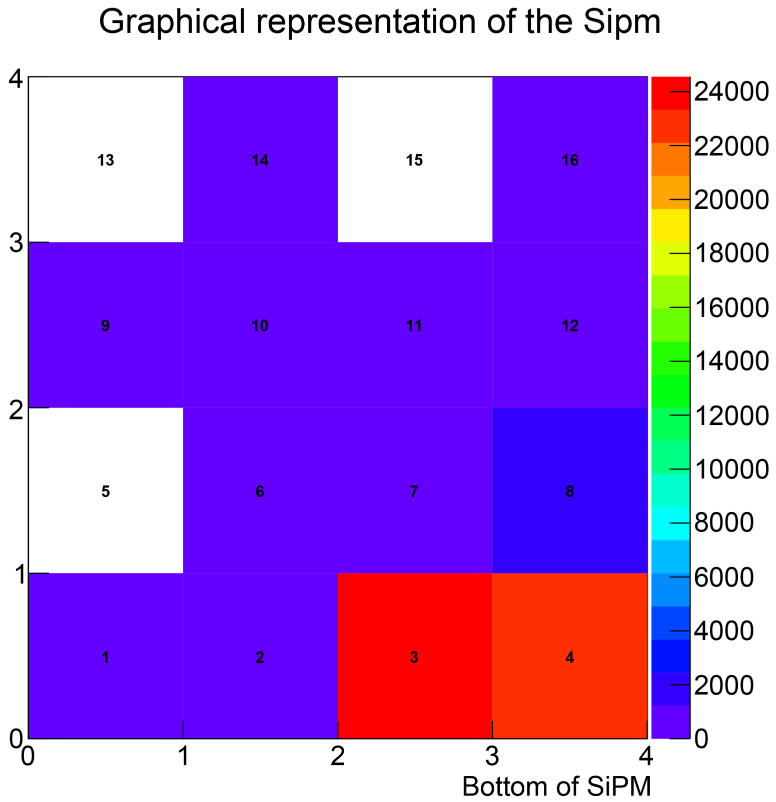

(b) 2D plot for coincidences seen by the SiPM array

Figure 5.3: Measurements recorded by moving the source to the bottom right of the SiPM array. The channels of the SiPM array are marked from 1 to 16.

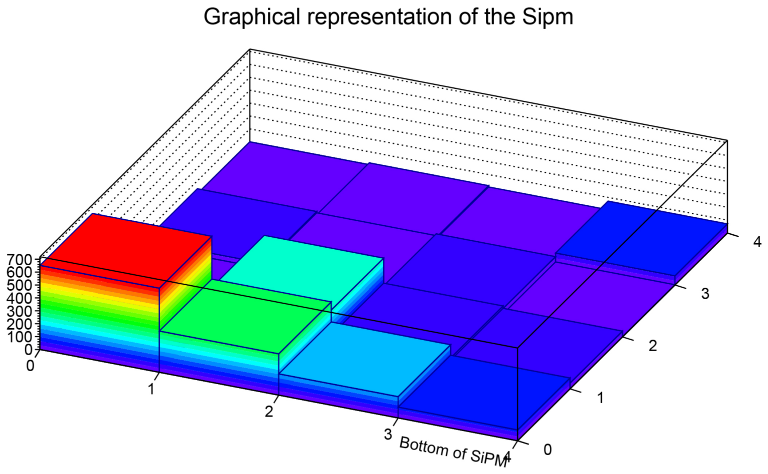

(a) 3D plot for coincidences seen by the SiPM array

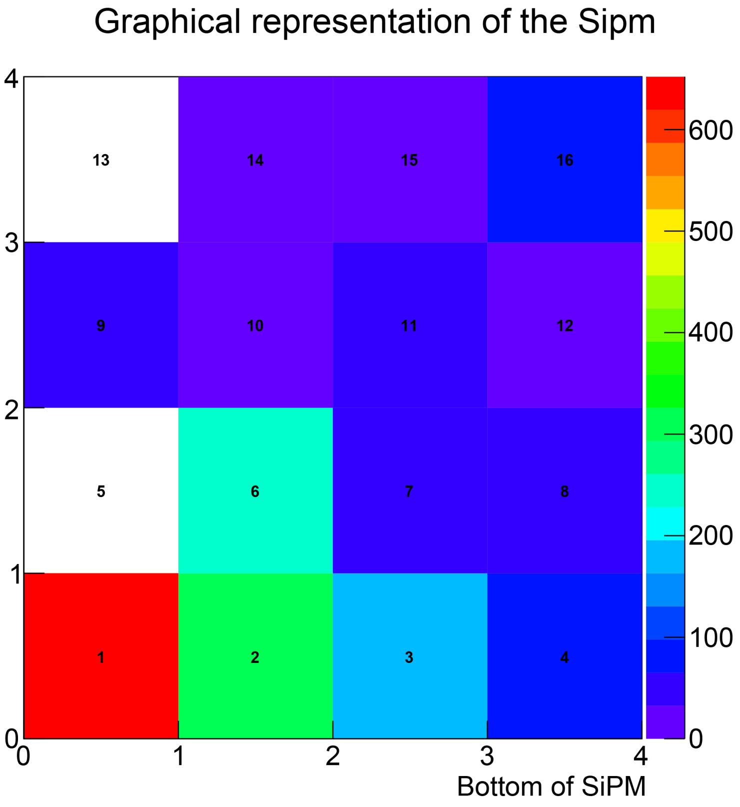

(b) 2D plot for coincidences seen by the SiPM array

Figure 5.4: Measurements recorded by moving the source to the bottom left of the SiPM array

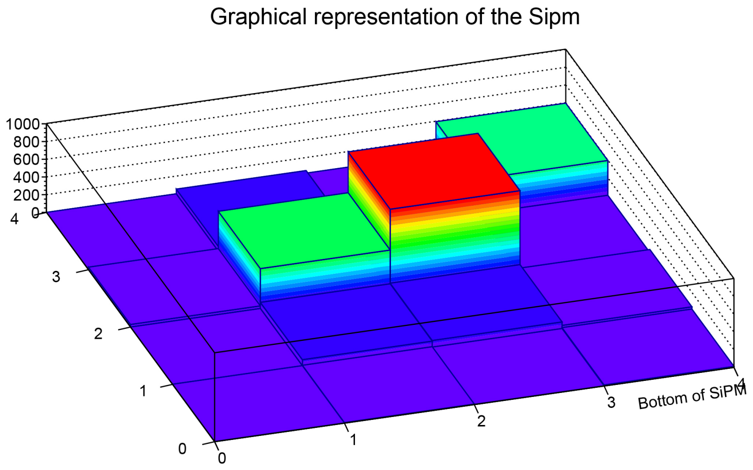

(a) 3D plot for coincidences seen by the SiPM array

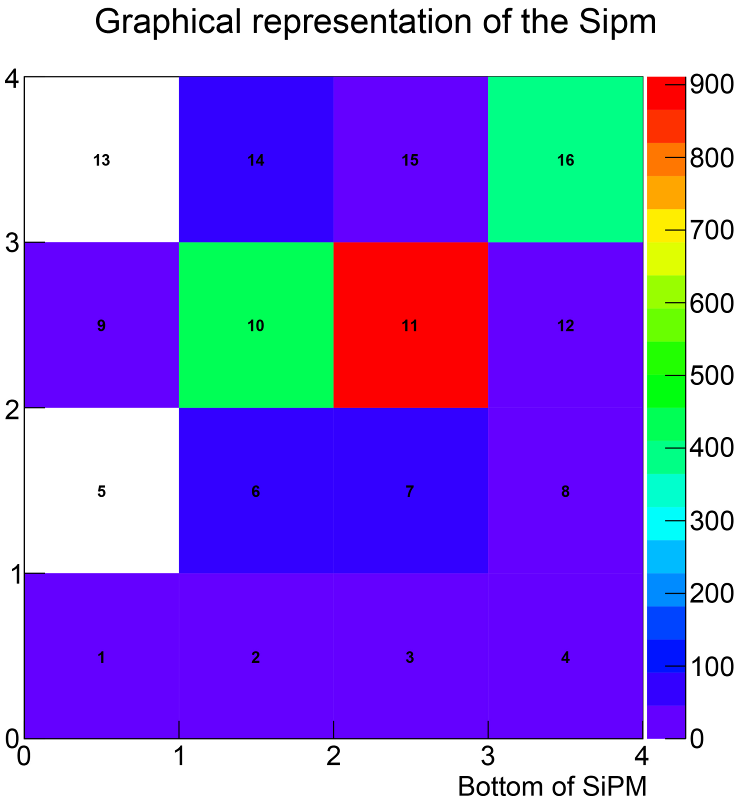

(b) 2D plot for coincidences seen by the SiPM array

Figure 5.5: Measurements recorded by moving the source to the bottom left of the SiPM array

5.2 Oscilloscope Measurements

Due to technical difficulties with the STiC3 chip, the focus was shifted towards taking measurements using an oscilloscope setup.

5.2.1 LED Measurements

To test if the oscilloscope was able to measure low light signals from the SiPM array without any preamplifier, it was first tested with the help of a simple LED. The LED was made to shine on the SiPM array and an external trigger was set by the pulse powering the LED. The waveforms of one channel were written to file whenever there was a trigger event and in such a way 4000 waveforms were recorded.

For the measurement, an ultravoilet LED, with a breakdown voltage of 2.3 V, was set to operate at 2.4 V and a frequency of 10 kHz. The purpose of setting such a low voltage was to get as low of a signal as possible on the SiPM. The SiPM array had a V_{bias} of 56.5 V, which corresponded to approximately 4 V overvoltage on all channels of the array. The signal as seen on the oscilloscope can be seen in figure 5.6. The level for the external trigger was set at 750 mV as shown in figure 5.6.

An analysis script was set up by the group using ROOT, which was capable of plotting a peak integral histogram for all the waveforms after making certain baseline correction and rejection to cut off noisy signals. The baseline correction shifted all waveforms to the same voltage level while the baseline rejection was done by taking 90 ns of data before all trigger events and then rejecting all waveforms which had a baseline RMS larger than a threshold value. The threshold value was set to be decided by the user and was chosen to be 0.5 mV. The choice of the threshold value was somewhat arbitrary and was taken to minimize contribution from signals that had a high baseline fluctuation. Another important thing to note here is that the peak integral corresponds to the amount of deposited charge per waveform and is given in the units of (V*ns). Dividing the obtained value by the voltage that enabled this drop would give the charge measured in pC.

As seen in figure 5.7, the peak integral histogram showed that a large amount of signals in the range of 1 to 2 pe levels were observed. This meant that the oscilloscope was able to record and differentiate between signals of different photon levels and an average number of photons detected could be assigned to each measured signal.

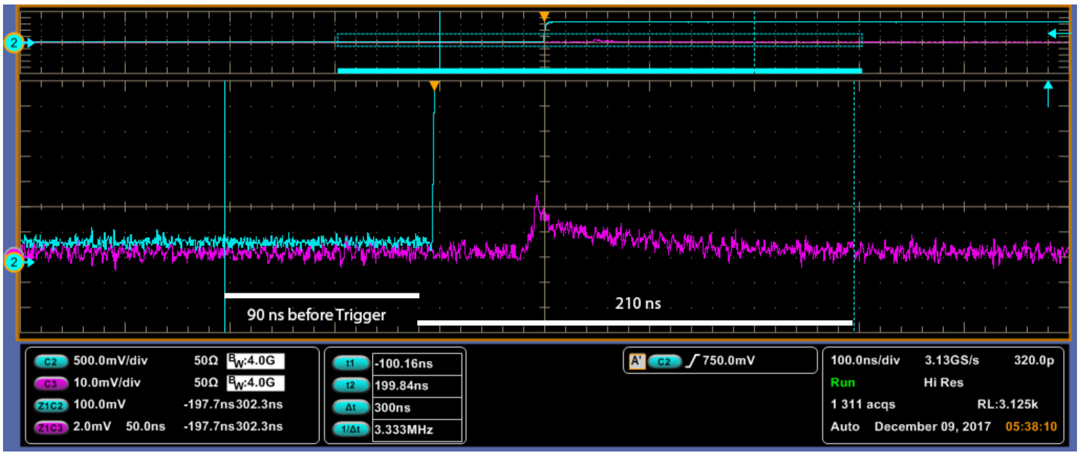

C2 500.0mV/div 50Ω BW:4.0G
C3 10.0mV/div 50Ω BW:4.0G
Z1C2 100.0mV -197.7ns 302.3ns
Z1C3 2.0mV 50.0ns -197.7ns 302.3ns

t1 -100.16ns
t2 199.84ns
Δt 300ns
1/Δt 3.333MHz

A' C2 750.0mV

100.0ns/div 3.13GS/s 320.0p
Run Hi Res
1 311 acqs RL:3.125k
Auto December 09, 2017 05:38:10

Figure 5.6: Screenshot of a single SiPM signal (purple) when there was a signal from the external trigger i.e. the pulse generator (blue), which was also powering the LED. Each division for the SiPM signal is of 2 mV.

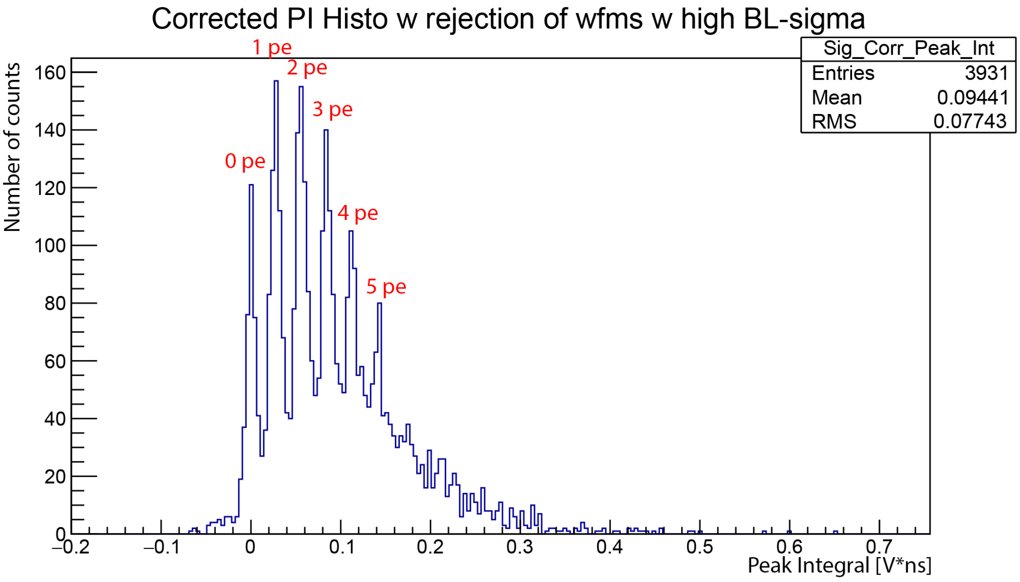

Figure 5.7: Histogram of an UV LED Peak Integral spectra of 4,000 waveforms recorded from the oscilloscope. Each photon event peak in the histogram is marked.

5.2.2 PMMA Measurements

For the detection of actual Cherenkov light, a plastic was needed which had the following properties:

- Low density
- high Z
- high refractive index
- low scintillation light
- high transmittance rate in UV and visible light range.

These properties were chosen to maximize the Cherenkov light yield from a material while having the lowest amount of scintillation light. The low density will ensure low electron scattering whereas the high refractive index will give more Cherenkov light. For this purpose, different materials were tested in the group for their scintillation light yield as most optic manufacturers do not quantize that quantity. Out of the materials tested, PMMA had the lowest scintillation light yield [44]. The chemical and optical properties of PMMA can be seen in Appendix B.

Calibration Measurement

The first measurement was taken with a 3 mm thick PMMA optically coupled to the SiPM array, that had a V_{bias} of 56.5 V, with the help of an optical gel. The collimated ^{90}Sr source was positioned in the middle of two channels and both of these channels were read out on the oscilloscope. The radioactive source was at a distance of 13 mm from the PMMA surface after collimation, which resulted in an electron beam which was not collimated but rather diverged in a circular area. For a point source, the radius of the circular area illuminated by the beam was calculated to be 2.58 mm. For the real ^{90}Sr source, this distance only increases as the source is not point-like, meaning that approximately an entire channel of the SiPM was covered by the electron beam.

Out of the two channels being fed to the oscilloscope, one channel was used as the trigger channel while the waveform from the other was written to file whenever there was a trigger event on the first channel higher than 3 mV. This way, events which were coincident on both channels contributed to the non-pedestal peaks in the peak integral spectra. 20,000 waveforms were recorded for statistics and then plotted in peak integral histograms after baseline correction to see if we saw any coincident light being detected on the SiPM array.

Theoretical Estimation of Photons Produced

Assuming max $\beta = 0.923$ (Appendix C), we can roughly calculate the number of Cherenkov photons created per track length if we also assume the SiPM to have 100% PDE by using equation 2.19. Since the detector was Silicon based, the energy range is cut between the range of 1.55 eV to 3.54 eV [4]. So, the number of photons emitted per unit length were calculated to be:

$$\frac{dN}{dx} = 73.59\,\frac{1}{\text{mm}}\left(1 - \frac{1}{\beta^2\,n^2}\right) = 34.68\,\text{mm}^{-1} \tag{5.1}$$

So, for a PMMA of 3 mm and a SiPM having a max PDE of 40%, approximately 41.61 photons for the whole length of the plastic were expected for 1.5 MeV source. Therefore, most events on the SiPM surface should be contributed from lower photon counts as the PDE of the SiPM array varies with wavelength and the ^{90}Sr source has an emission spectra (see Appendix A and C).

Results

The peaks in figure 5.8 and 5.9 indicate the detection of Cherenkov light as most events occurred due to 1 or 2 photons. Of course there might have been some contribution due to scintillation light as there are distinct peaks that go up to 6 pe level or more. These results were then used to get a relation between the peak integral, which is the amount of charge deposited, and photon number. This was done by fitting each individual photon event peak with a Gaussian to obtain the mean value and then plotting the said mean against the peak number as shown in figure 5.10 and 5.11 respectively.

The resulting plot showed a linear relation between the charge deposited and the corresponding photon peak. This was an expected result as increasing number of photons deposit more charge on a single SiPM channel and is dependent only on the overvoltage being provided to the SiPM array. From this graph, average number of photons on a single channel was calculated by measuring the average charge deposited on that channel. This calibration was then done for all other channels by assuming that all 16 channels on the SiPM array shared approximately the same breakdown voltage as indicated by Hamamatsu.

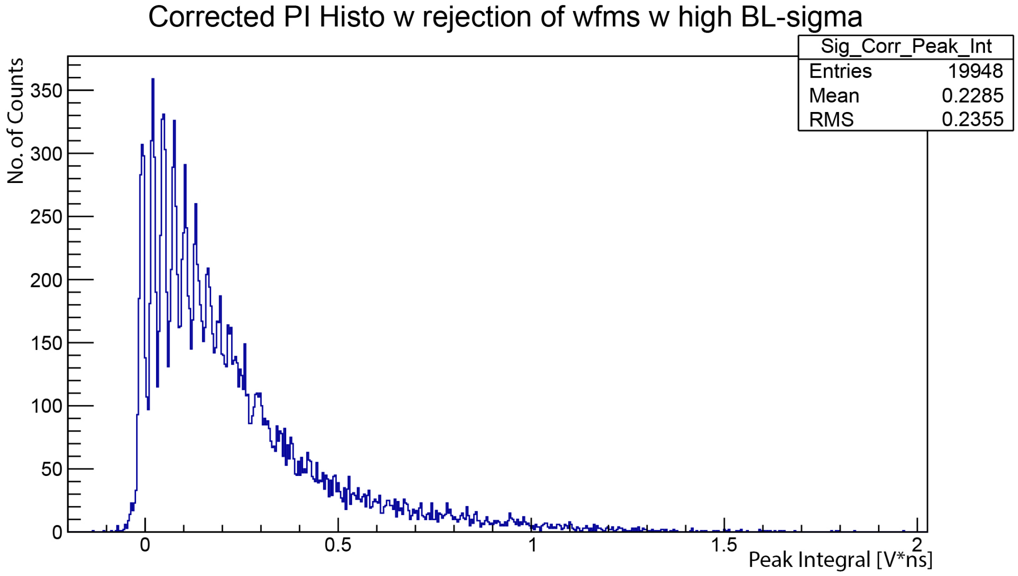

Figure 5.8: Histogram of 3 mm thick PMMA Peak Integral spectra of 20,000 waveforms recorded from the oscilloscope.

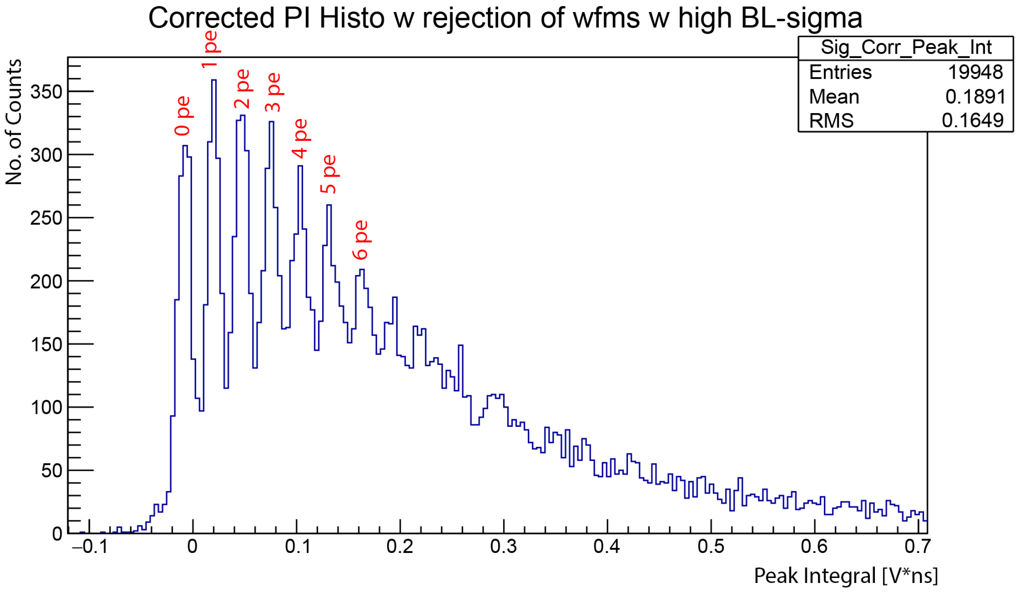

Figure 5.9: Zoomed in version of figure 5.8, where each photo equivalent peak is marked.

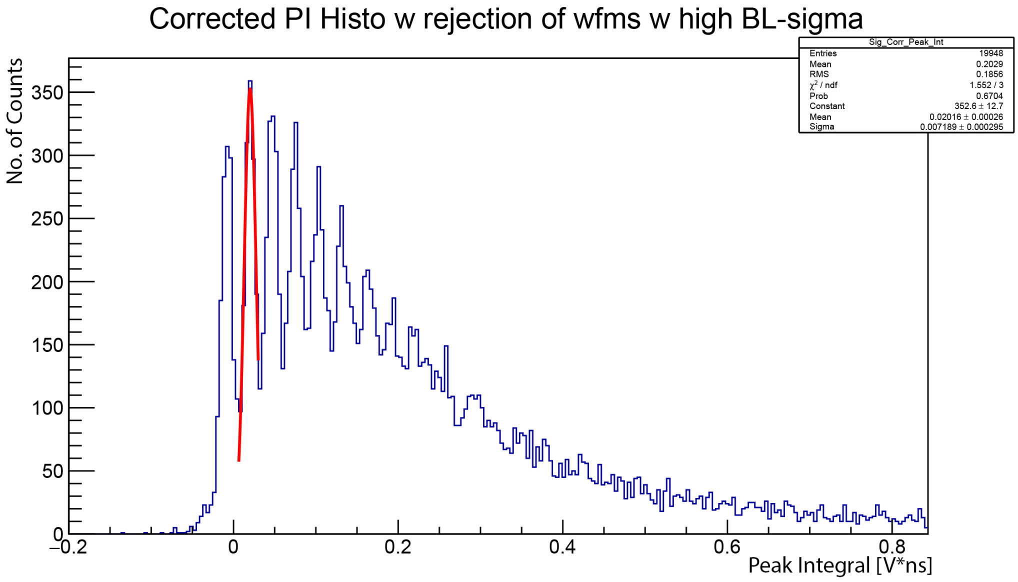

Figure 5.10: Gaussian fit on 1 pe peak of 3 mm PMMA. The fit was applied up to the 6 pe peak to get the mean values of each peak.

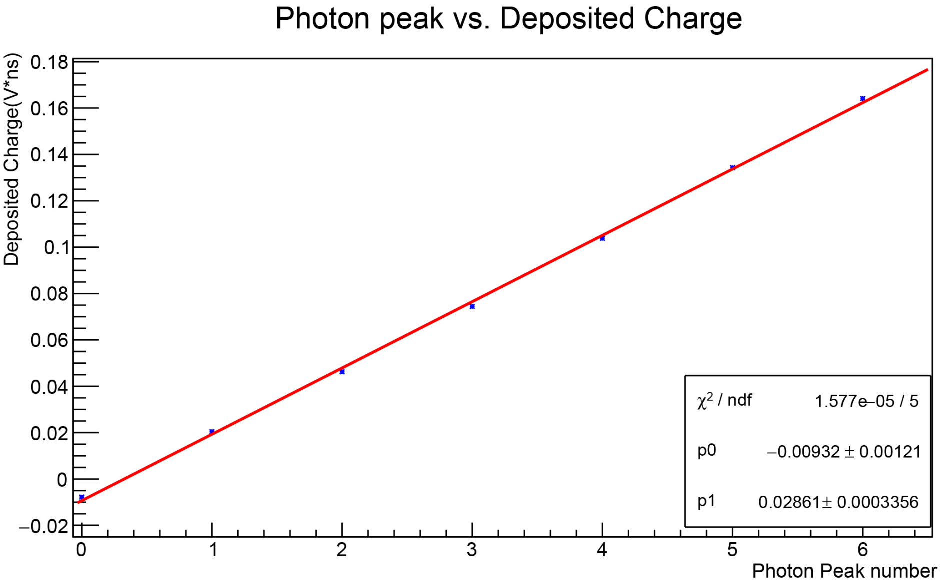

Figure 5.11: Charge deposited vs. photon peak number for a single SiPM channel fitted with a linear fit, where p0 is the intercept and p1 is the slope.

Measurement 1

After seeing agreeable results, the setup was expanded to take measurements over all 16 channels of the SiPM array with a 3 mm PMMA on top at V_{bias} of 56.5 V. The ^{90}Sr source was pointed towards the center of the SiPM array. Since the oscilloscope could only read 4 channels at a time, one channel was selected as the trigger channel (B3 or channel 7 in figure 5.12 (b)) for all readings. While keeping the trigger channel constant at 3 mV, 10,000 waveforms from all other channels were read out in groups of three whenever there was a trigger event at channel 7. Afterwards, one last reading was taken by taking channel 6 as the trigger and reading out the data from channel 7. This was done to get a more accurate estimation of the average photon count on channel 7 as otherwise the channel would only show high photon counts because the trigger was set at 3 mV, which corresponded to 2-3 pe events.

The data was combined for all 16 channels of the SiPM array and by using the calibration curve from figure 5.11, average photon number for all channels was calculated and plotted in a 2D color intensity plot and 3D lego plot, as shown in figure 5.12.

The discrepancy between the difference in average photon number in the neighboring channels at the center of the SiPM array can be explained by two possibilities:

- The Source was not pointed at the exact center of the SiPM array
- Due to collimation and distance of the source from the PMMA, the electron beam was not centered on a point at the plastic but rather diverged

Even though a step motor was used to move the source, the initial placement of the source to make it point at the center of the array was done by eye. Therefore, the centering procedure was prone to some parallax effect that was caused by human interaction. Also, as the source was collimated with an aluminum plate with a hole and had a distance of 13 mm from the PMMA, some unwanted divergence of the beam was observed that resulted in a wider beam size on the PMMA surface. This effect was due to the limitation of the setup which prevented the source from being closer to the radiator material. This error can be reduced by moving the source closer to the PMMA surface or designing an additional collimator setup which is attached to PMMA instead of the source.

Nonetheless, the results were highly promising as the center channels showed a higher average photon count than the rest of the SiPM array.

Measurement 2

For the second measurement with the 3 mm PMMA, the source was moved -4.5 mm in the y direction from the center such that the Cherenkov cone fell on channels 2, 3, 6 and 7 of the SiPM array. The measurement procedure was kept the same as the previous measurement.

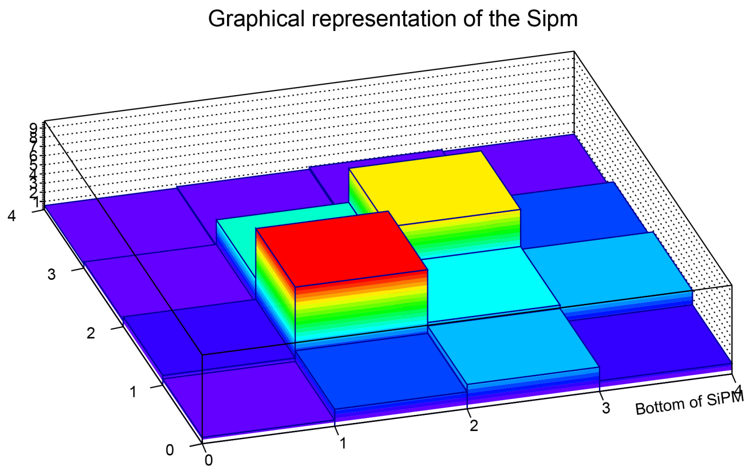

(a) 3D plot for average photon count seen by the SiPM array

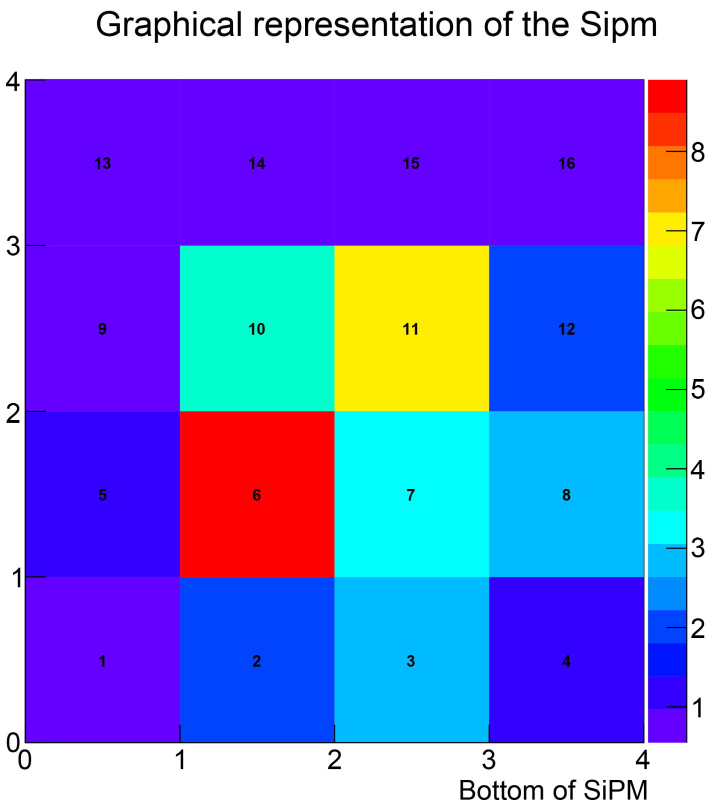

(b) 2D plot for average photon count seen by the SiPM array

Figure 5.12: Measurements recorded with the source in the center of the SiPM array with 3 mm PMMA. The color intensity and height of the 3D lego plot represent the average photon number for the channel.

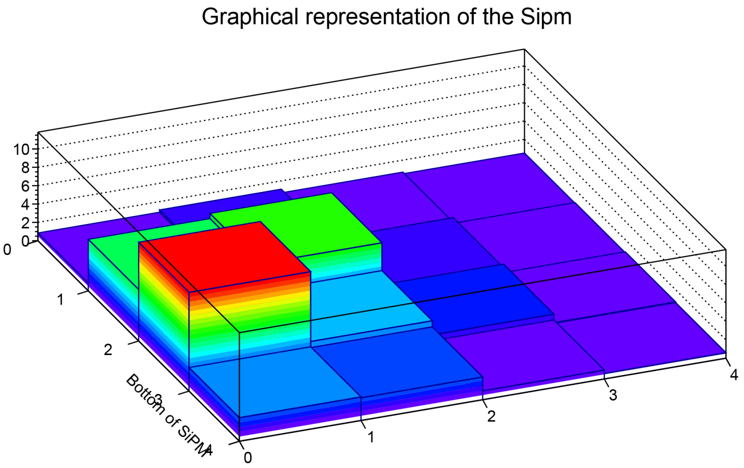

(a) 3D plot for hits seen by the SiPM array

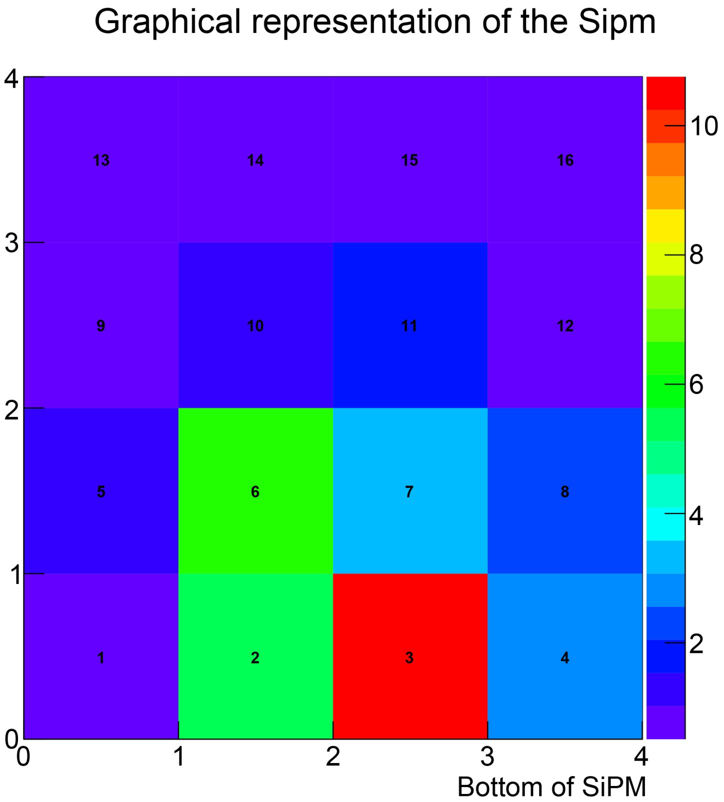

(b) 2D plot for hits seen by the SiPM array

Figure 5.13: Measurements recorded with the source pointed at the bottom half of the SiPM array with 3 mm PMMA. The color intensity and height of the 3D lego plot represent the average photon number for the channel.

The result of the measurement are shown in figure 5.13. The increased average photon count for channel 2, 3, 6 and 7 indicated that most counts were detected on those channels, which is what was expected. Using these results, it was concluded that the movement of the average photon count on the channels was due to the movement of the resulting Cherenkov cone which changed position due to the movement of the radioactive source.

Measurement 3

To test if the aforementioned conclusion was correct, more measurements were taken by moving the source back to the center of the array and swapping out the 3 mm PMMA sample with a thicker 6 mm one. The measurement procedure was kept the same as the previous two measurements to make them comparable to each other, even though a bigger Cherenkov circle radius was expected.

Theoretically, changing the thickness of PMMA would result in more photons being detected in the outer parts of the array than before as due to increase in thickness of the plastic, the maximum radius of the Cherenkov cone should also increase.

Figure 5.14 and figure 5.15 show the results of the measurements when the source was centered and moved -4.5 mm in the y direction respectively. As seen, the radius of the Cherenkov circle increased in size when compared to the results shown in figure 5.12 and 5.13. The movement of the Cherenkov circle confirmed the hypothesis that the photons being detected were indeed part of the Cherenkov circle as the movement of the source translated to the movement of the circle. However, these results also confirmed the earlier suspicions that the source was not initially positioned in the exact center of the SiPM array by eye. This explained the Cherenkov cone being detected in the lower half of the array rather than the exact center. As when the source was moved, the Cherenkov circle moved downwards with the average photon count increasing in channels 2 and 3 (figure 5.15). The increased average photon count in the central channels could also be explained due the beta energy spectrum of the source not having any distinct peak and having more emissions in the lower energy range (see Appendix C). This means that the channels where the source was centered would see more average photon number since the opening angle of the Cherenkov cone in the lower range would be small which would lead to smaller radii circles.

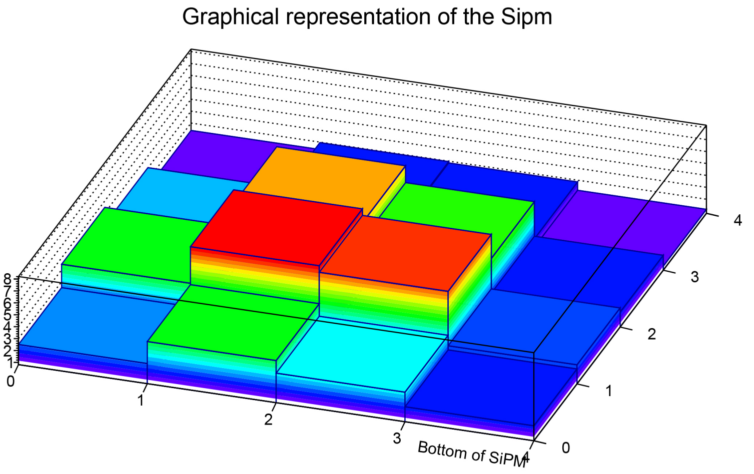

(a) 3D plot for average photon count seen by the SiPM array

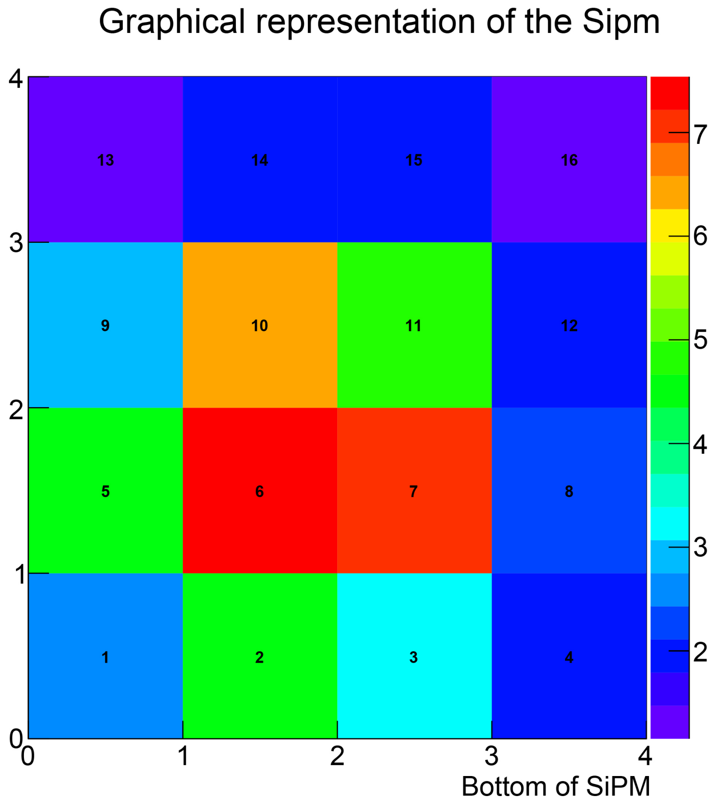

(b) 2D plot for average photon count seen by the SiPM array

Figure 5.14: Measurements recorded with the source in the center of the SiPM array with 6 mm PMMA. The color intensity and height of the 3D lego plot represent the average photon number for the channel.

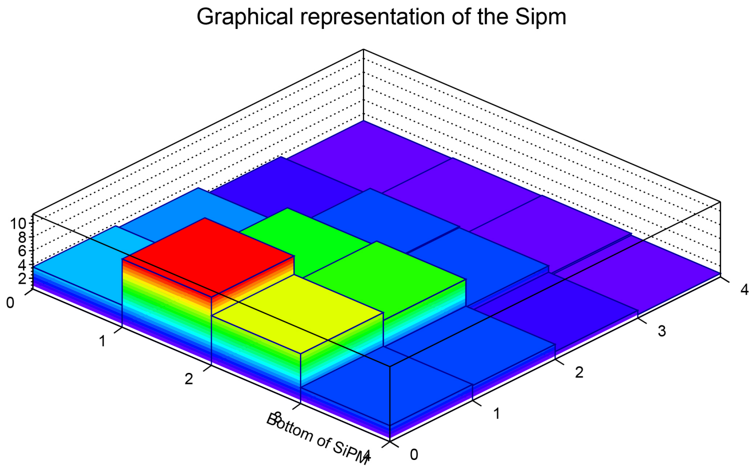

(a) 3D plot for average photon count seen by the SiPM array

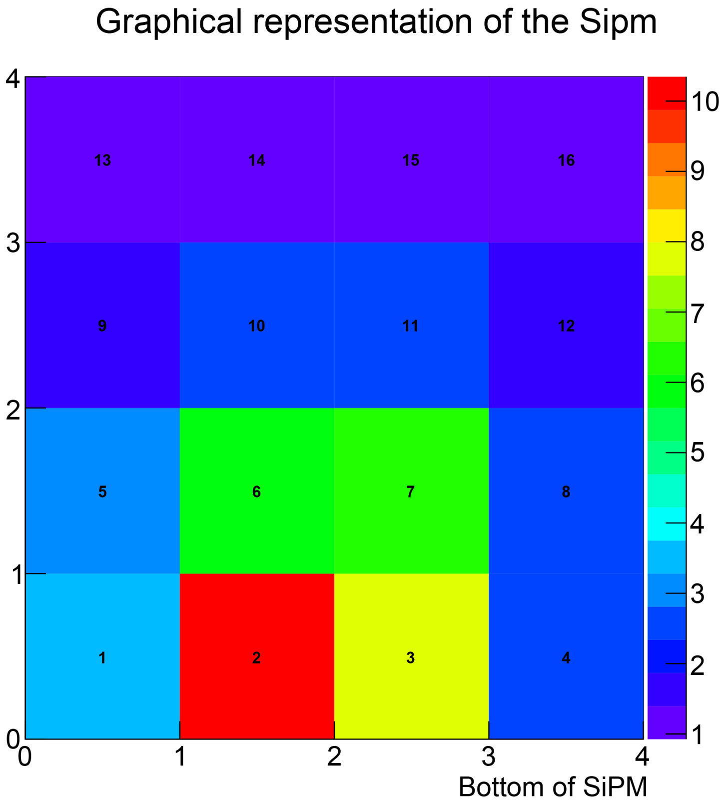

(b) 2D plot for average photon count seen by the SiPM array

Figure 5.15: Measurements recorded with the source moved -4.5 mm towards the bottom of the SiPM array with 6 mm PMMA. The color intensity and height of the 3D lego plot represent the average photon number for the channel.

5.2.3 TPX^{TM}Measurements

Some preliminary measurements were also taken by substituting the 3 mm PMMA with another plastic material called TPX^{TM} from Mitsui Chemicals. Key optical and chemical properties of TPX can be viewed in Appendix B. This material was chosen due to the manufacturer's promise of it having a higher transmission percentage in the UV range.

Data was collected by optically coupling TPX to the SiPM array and focusing the collimated ^{90}Sr source on top of two channels which were then fed to the oscilloscope. One channel was set to act as the trigger channel with a trigger level of 3 mV and the waveform from the other channel was written to file whenever there was an event. 20,000 waveforms were collected for statistics and their peak integral histogram was plotted after a baseline rejection 0.5 mV as shown in figure 5.10.

Comparing figure 5.16 with 5.9, it is clear that there are far fewer high pe events in TPX than in PMMA. Therefore, further studies by substituting different radiator materials can be beneficial for the experiment as more events are seen due to the contribution of 1 and 2 photons. This indicates that TPX emits less scintillation light than PMMA. However due to the lack of ease of availability of the material, further measurements by increasing the thickness of the material could not be conducted at this time.

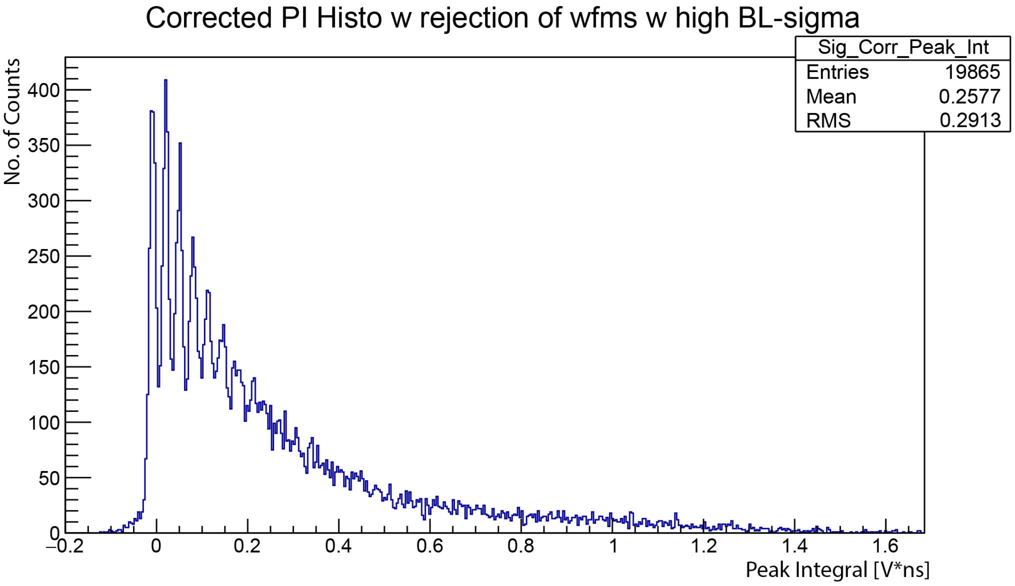

Figure 5.16: Histogram showing the peak integral of 20,000 waveforms collected by shining a ^{90}Sr source on top of a SiPM channel coupled to 3 mm thick TPX.

Chapter 6

Conclusion and Outlook

Within the scope of this thesis, the coincident detection of Cherenkov photons using SiPMs coupled optically with PMMA or some other plastic was observed. Some initial simulation studies were also done for the reconstruction of the Cherenkov circles. The validity of CHT for finding the radius of the circles was tested. Given the recent formation of the group, some preliminary work regarding lab setup, measurement methods and analysis scripts was also done in collaboration with colleagues.

Initial studies into the reconstruction of the Cherenkov circles for their radius using CHT was done in the start of the thesis while setting up a proper measurement setup in the lab. The simulations done in MATLAB showed promising results which suggested that CHT was indeed a valid technique for the detection of circles generated by randomly distributed photons, on a limited resolution detector. These results agreed with previous simulations done in [4]. However, further studies did suggest the need for several improvements in the algorithm before it could be employed for ellipse detection.

The main focus of the thesis was towards the detection of Cherenkov photons using SiPMs. For this purpose, two measurement setups were used. Using the STiC3 ASIC chip initial measurements were taken with 3 mm PMMA. For the analysis of these measurements, a ROOT based analysis program was designed in collaboration with colleagues. The initial measurements showed the setup could indeed be used for the coincident detection of Cherenkov light for events higher than 1 pe level. The results also pointed towards the need for some further calibration of the STiC3 chip triggering system. Before any such calibration could be made, the STiC3 chip ran into technical problems making it unusable for the remainder of this thesis.

To continue further measurements after the STiC3 setup became unusable, an oscilloscope was employed. Measurements taken showed promising results as Cherenkov photons could certainly be detected on the SiPM surface along with some contribution from scintillation light emitting from the PMMA. To confirm the photons detected were indeed from Cherenkov radiation, more measurements were taken by varying the thickness of PMMA from 3 mm to 6 mm and moving the ^{90}Sr source with both thicknesses. The results were promising and showed that the detection of Cherenkov photons with a radiator material on top of a SiPM was possible. This could be taken as a very initial proof of principle towards calculating the electron source position using Cherenkov photons. The results also highlighted some of the limitations of the current measurement setup such as the need for a better initial positioning system and an additional collimator for the source.

The next steps for improving the results would be to design and use an additional collimator setup that limits the distance between the source and the radiator material. The additional setup should also be capable of increasing the accuracy when trying to center the source over the SiPM array. Data taken by such an apparatus would provide better results. Further steps would also include analyzing data taken from PMMA samples of varying thicknesses as well as testing different radiator materials to find more suitable candidates than PMMA. As measurements done using TPX over PMMA showed that TPX emitted lower scintillation light than PMMA and serve towards the ultimate goal of developing a Compton-Cherenkov based imaging system.

Appendix A

S13361-3075AS

A.1 PDE vs. Wavelength

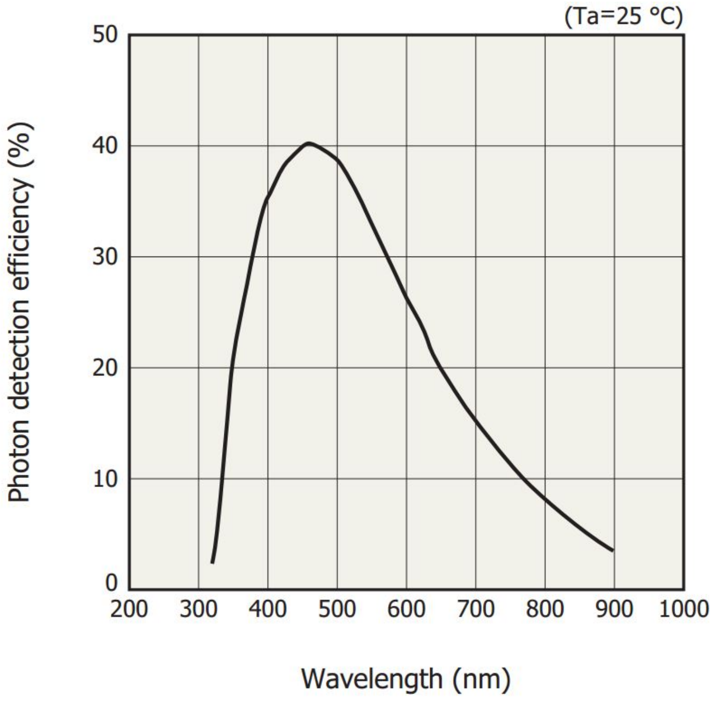

Figure A.1: Graph showing the photon detection efficiency (PDE) of the SiPM at various wavelengths. Taken from [38].

A.2 Overvoltage vs. Gain

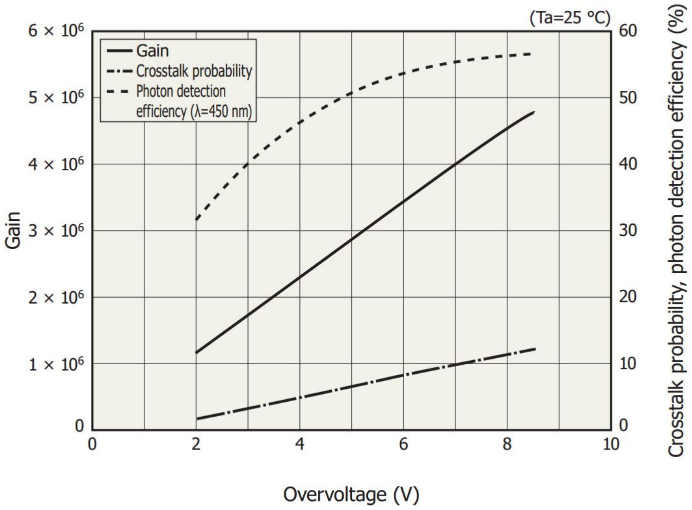

Figure A.2: Graph showing the effect on the Gain, PDE and Crosstalk as the overvoltage is increased [38].

Appendix B

Radiator Material Properties

B.1 PMMA

Chemical Name

Poly(methyl methacrylate)

Chemical and Optical Properties

Density	1.18	g/cm^3
Refractive Index	1.49	-
Light Transmission at 400 nm	92	%
Transmission Range	380 - 1200	nm

Table B.1: Table showing the key chemical and optical properties of PMMA which are relevant to the experiment. Taken from [45] and [46].

B.2 TPX^{TM}

Chemical Name

Polymethlypentene

Chemical and Optical Properties

Density	0.833	g/cm^3
Refractive Index	1.462	-
Light Transmission at 400 nm	94	%
Transmission Range	280 - 1200	nm

Table B.2: Table showing the key chemical and optical properties of TPX which are relevant to the experiment. Taken from [46].

B.3 Comparison between PMMA and TPX Transmittance Range

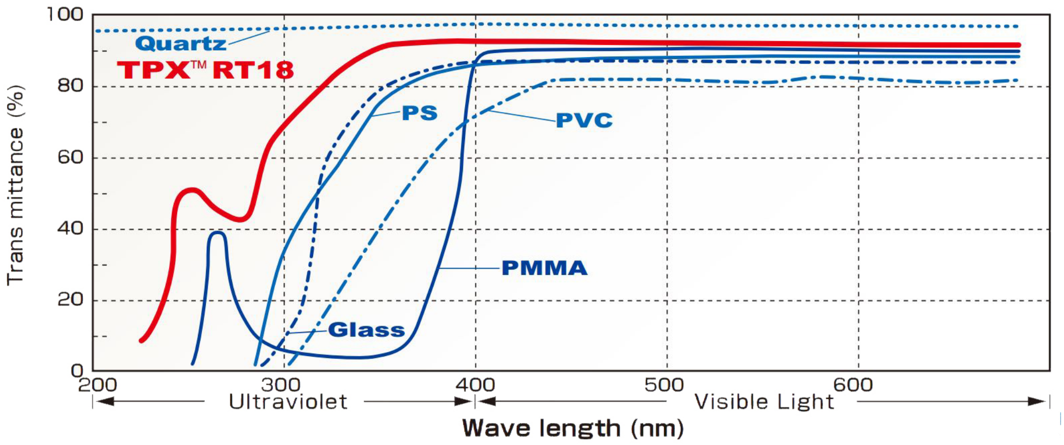

Figure B.1: Comparison of the transmittance ranges of different materials. Taken from [46].

Appendix C

Beta Spectra of ^{90}Sr

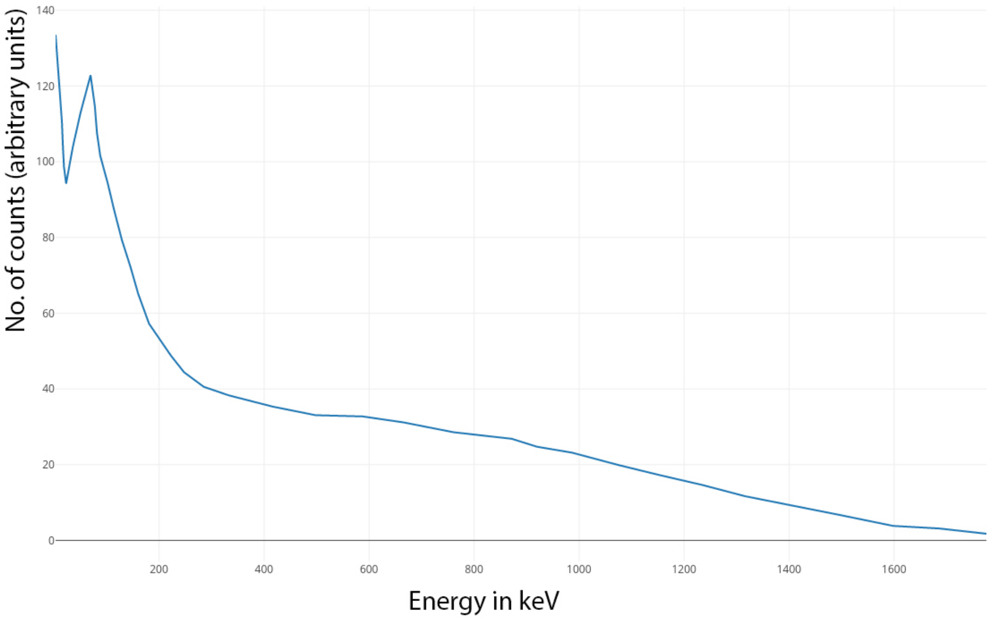

Figure C.1: β spectra of ^{90}Sr obtained from a scintillation counter. The Y axis denotes the number of counts on the counter and are in arbitrary units. Adapted from [47]

Bibliography

[1] K. E. Baidoo, K. Yong, and M. W. Brechbiel. Molecular pathways: Targeted -particle radiation therapy. *Clinical Cancer Research*, 19(3):530–537, dec 2012.

[2] Gary W. Phillips. Gamma-ray imaging with compton cameras. *Nuclear Instruments and Methods in Physics Research Section B: Beam Interactions with Materials and Atoms*, 99(1-4):674–677, may 1995.

[3] M Fontana, D Dauvergne, J M Ltang, J-L Ley, and Testa. Compton camera study for high efficiency spect and benchmark with anger system. *Physics in Medicine & Biology*, 62(23):8794, 2017.

[4] A. H. Walenta, A. B. Brill, T. Conka-Nurdan, I. Fleck, L. R. Furenlid, and T. E. Peterson. *GamSim A windows-based simulation tool for gamma-ray detector development.* IEEE, Oct 2016.

[5] T. E. Peterson, A. B. Brill, and A. H. Walenta. *High energy gamma-ray imaging using Cherenkov cone detection - A Monte Carlo study with application to a Compton camera system.* IEEE, Oct 2012.

[6] Shinichiro Takeda, Yuto Ichinohe, Kouichi Hagino, Hirokazu Odaka, Takayuki Yuasa, Shin nosuke Ishikawa, Taro Fukuyama, Shinya Saito, Tamotsu Sato, Goro Sato, Shin Watanabe, Motohide Kokubun, Tadayuki Takahashi, Mitsutaka Yamaguchi, Hiroyasu Tajima, Takaaki Tanaka, Kazuhiro Nakazawa, Yasushi Fukazawa, and Takashi Nakano. Applications and imaging techniques of a si/cdte compton gamma-ray camera. *Physics Procedia*, 37(Supplement C):859 – 866, 2012. Proceedings of the 2nd International Conference on Technology and Instrumentation in Particle Physics (TIPP 2011).

[7] C. Patrignani and Particle Data Group. Review of particle physics. *Chinese Physics C*, 40(10):100001, 2016.

[8] William R. Leo. *Techniques for Nuclear and Particle Physics Experiments.* Springer Berlin Heidelberg, 1994.

[9] Claus Grupen and Boris Shwartz. *Particle Detectors (Cambridge Monographs on Particle Physics, Nuclear Physics and Cosmology).* Cambridge University Press, 2008.

[10] A. O. Hanson, L. H. Lanzl, E. M. Lyman, and M. B. Scott. Measurement of multiple scattering of 15.7-mev electrons. *Phys. Rev.*, 84:634–637, Nov 1951.

[11] Yung-Su Tsai. Pair production and bremsstrahlung of charged leptons. *Rev. Mod. Phys.*, 46:815–851, Oct 1974.

[12] G. Moliére. Theorie der streuung schneller geladener teilchen ii , mehrfach- und vielfachstreuung. *Z. Naturforschg.*, 3a:78–97, 1948.

[13] L. Meyer. Plural and multiple scattering of low-energy heavy particles in solids. *Physica Status Solidi (b)*, 44(1):253–268, mar 1971.

[14] H. A. Bethe. Molière's theory of multiple scattering. *Phys. Rev.*, 89:1256–1266, Mar 1953.

[15] Jamil Lambert, Yongbai Yin, David R. McKenzie, Sue Law, and Natalka Suchowerska. Cerenkov light spectrum in an optical fiber exposed to a photon or electron radiation therapy beam. *Appl. Opt.*, 48(18):3362–3367, Jun 2009.

[16] J.W. LeBlanc, N.H. Clinthorne, C. Hua, W.L. Rogers, D.K. Wehe, and S.J. Wilderman. A compton camera for nuclear medicine applications using 113min1. *Nuclear Instruments and Methods in Physics Research Section A: Accelerators, Spectrometers, Detectors and Associated Equipment*, 422(1):735 – 739, 1999.

[17] W Rogers, Neal Clinthorne, and A Bolozdynya. Compton cameras for nuclear medical imaging, 12 2004.

[18] J.B. Martin, N. Dogan, J.E. Gormley, G.F. Knoll, M. O. Donnell, and D.K. Wehe. Imaging multi-energy gamma-ray fields with a compton scatter camera. *IEEE Transactions on Nuclear Science*, 41(4):1019–1025, 1994.

[19] R. Dolenec, H. Chagani, S. Korpar, P. Krian, R. Pestotnik, and A. Stanovnik. Tests of a silicon photomultiplier module for detection of cherenkov photons. *Nuclear Instruments and Methods in Physics Research Section A: Accelerators, Spectrometers, Detectors and Associated Equipment*, 628(1):398 – 402, 2011. VCI 2010.

[20] Slawomir Piatek. A technical guide to silicon photomultipliers (sipm). Technical report, Hamamatsu Corporation & New Jersey Institute of Technology, January 2017.

[21] Ben Streetman and Sanjay Banerjee. *Solid State Electronic Devices (5th Edition)*. Prentice Hall, 1999.

[22] D Renker and E Lorenz. Advances in solid state photon detectors. *Journal of Instrumentation*, 4(04):P04004, 2009.

[23] K. A. Tadday. *Scintillation Light Detection and Applicatoin of Silicon Photomultipliers on Imaging Calorimetry and Positron Emission Tomography*. PhD thesis, Ruperto-Carola-University of Hidelberg, 2011.

[24] Gerhard Lutz. *Semiconductor Radiation Detectors: Device Physics*. Springer, 2007.

[25] Chen Xu. *Study of the Silicon Photomultipliers and Their Applications in Positron Emission Tomography.* PhD thesis, University of Hamburg, 2014.

[26] H. Otono, H. Oide, S. Yamashita, T. Yoshioka, K. Yamamoto, K. Yamamura, and K. Sato. Study of the internal mechanisms of Pixelized Photon Detectors operated in Geiger-mode. *ArXiv e-prints*, August 2008.

[27] Slawomir Piatek. Physics and operation of the mppc silicon photomultiplier. Technical report, Hamamatsu Corporation & New Jersey Institute of Technology, February 2014.

[28] Marco Ramilli. Characterization of SiPM: Temperature dependencies. In *2008 IEEE Nuclear Science Symposium Conference Record.* IEEE, oct 2008.

[29] Adam Nepomuk Otte, Distefano Garcia, Thanh Nguyen, and Dhruv Purushotham. Characterization of three high efficiency and blue sensitive silicon photomultipliers. *Nuclear Instruments and Methods in Physics Research Section A: Accelerators, Spectrometers, Detectors and Associated Equipment*, 846(Supplement C):106 – 125, 2017.

[30] A.L. Lacaita, F. Zappa, S. Bigliardi, and M. Manfredi. On the bremsstrahlung origin of hot-carrier-induced photons in silicon devices. *IEEE Transactions on Electron Devices*, 40(3):577–582, mar 1993.

[31] H.P.V. C. Method and means for recognizing complex patterns, December 18 1962. US Patent 3,069,654.

[32] P. E. Hart. How the hough transform was invented [dsp history]. *IEEE Signal Processing Magazine*, 26(6):18–22, November 2009.

[33] Gary Bradski and Adrian Kaehler. *Learning OpenCV: Computer Vision with the OpenCV Library.* O'Reilly Media, 2008.

[34] Harvey Rhody. Hough circle transform. URL: `https://www.cis.rit.edu/class/simg782/lectures/lecture_10/lec782_05_10.pdf`, October 11 2005.

[35] Suvrajit Maji and Marcel P. Bruchez. Inferring biological structures from super-resolution single molecule images using generative models. *PLOS ONE*, 7(5):1–10, 05 2012.

[36] David Young. Hough transform for circles. URL: `https://de.mathworks.com/matlabcentral/fileexchange/26978-hough-transform-for-circles`, May 2016.

[37] Siegmund Brandt. *Data Analysis: Statistical and Computational Methods for Scientists and Engineers.* Springer, 2014.

[38] Hamamatsu. *MPPC (Multi-Pixel Photon Counter) arrays - S13361-3050 series*, 8 2017.

[39] Hamamatsu. *MPPC and MPPC module for precision measurements*, 3 2016.

[40] Zhen-Xiong Yuan and Huangshan Chen. *STiC3 User Guide.* Kirchoff Institute for Physics, Heidelberg University.

[41] Tobias Harion. The stic asic high precision timing with silicon photomultipliers, 2015.

[42] T Harion, K Briggl, H Chen, P Fischer, A Gil, V Kiworra, M Ritzert, H C Schultz-Coulon, W Shen, and V Stankova. Stic a mixed mode silicon photomultiplier readout asic for time-of-flight applications. *Journal of Instrumentation*, 9(02):C02003, 2014.

[43] Patrick Eckert, Hans-Christian Schultz-Coulon, Wei Shen, Rainer Stamen, and Alexander Tadday. Characterisation studies of silicon photomultipliers. *Nuclear Instruments and Methods in Physics Research Section A: Accelerators, Spectrometers, Detectors and Associated Equipment*, 620(2):217 – 226, 2010.

[44] Hedia Bäcker. Detektion von tscherenkow-licht mit einer pmt, 10 2016.

[45] Laminated Plastics. *Technical Data Sheet Acrylic (PMMA).*

[46] Mitsui Chemicals. *TPX^{TM}Brochure*, 9 2011.

[47] LD Didactic. Strontium-90. `https://www.ld-didactic.de/software/524221en/Content/Appendix/Sr90.htm`. Accessed: 2010-09-30.

Acknowledgement

First of all, I would like to thank Prof. Ivor Fleck for not only giving me the opportunity to do my Master thesis in his group but also for being an outstanding supervisor. Thank you for your hands on approach, encouragement and guidance.

A big thank you goes to Ulrich Werthenbach for providing unconditional support and advise for the experiment as well as single handedly designing and printing essential tools needed for the experimental setup.

Thank you Reimund Bayerlein, for a lot actually. Not only did you help proof read this entire thesis, your analysis scripts helped make this whole thing possible. Thank you as well for your company during official trips, wonderful moments and advises you offered.

I would like to thank Ayman Salman for taking readings while I focused on writing my thesis and Ayesha Ali for her work in characterizing the SiPM.

Thanks a lot to the entire Electronics lab of University of Siegen for their amazing support for the whole project.

Thank you to Huangshan Chen and Vera Koleva Stankova for providing support for STiC3 and answering any and all questions we had about the device. On a similar note, thank you to Ole Brandt for not only providing additional, unreserved support but also for the fun memories and being our tour guide in Hamburg.

I would like to thank Wolfgang Walkowiak for his amazing IT support, teaching me how to properly use git repository, and answering networking and security questions. In extension, I would also like to thank the entire Experimental Particle Physics group at University of Siegen for the memories.

Also, thank you to my gaming buddies who kept me from going insane and by that logic, thank you to Gaben as well. Thanks to the “RUNG” group and my travel companions for the great memories, food and company.

Finally, a big thank you goes out to my friends (even those who went back to being strangers again), fraternity and family for their unconditional support and providing me with the push I required in certain situations.

Erklärung

Hiermit erkläre ich, dass ich die vorliegende Masterarbeit selbstndig verfasst und keine anderen als die angegebenen Quellen und Hilfsmittel benutzt sowie Zitate und Ergebnisse Anderer kenntlich gemacht habe.

Siegen, den February 12, 2018

Waleed Khalid